



# Impact of atmospheric coastal jet off central Chile on sea surface temperature from satellite observations (2000-2007)

Lionel Renault, Boris Dewitte, Mark Falvey, René Garreaud, Vincent Echevin, Fabrice Bonjean

## ► To cite this version:

Lionel Renault, Boris Dewitte, Mark Falvey, René Garreaud, Vincent Echevin, et al.. Impact of atmospheric coastal jet off central Chile on sea surface temperature from satellite observations (2000-2007). *Journal of Geophysical Research*, 2009, 114 (C08006), pp.22. 10.1029/2008JC005083 . hal-00765740

**HAL Id: hal-00765740**

**<https://hal.science/hal-00765740>**

Submitted on 10 Jun 2014

**HAL** is a multi-disciplinary open access archive for the deposit and dissemination of scientific research documents, whether they are published or not. The documents may come from teaching and research institutions in France or abroad, or from public or private research centers.

L'archive ouverte pluridisciplinaire **HAL**, est destinée au dépôt et à la diffusion de documents scientifiques de niveau recherche, publiés ou non, émanant des établissements d'enseignement et de recherche français ou étrangers, des laboratoires publics ou privés.

## Impact of atmospheric coastal jet off central Chile on sea surface temperature from satellite observations (2000–2007)

Lionel Renault,<sup>1</sup> Boris Dewitte,<sup>1,2</sup> Mark Falvey,<sup>3</sup> René Garreaud,<sup>3</sup> Vincent Echevin,<sup>4</sup> and Fabrice Bonjean<sup>5</sup>

Received 8 August 2008; revised 31 March 2009; accepted 28 April 2009; published 12 August 2009.

[1] The coast of central Chile is characterized by intermittent low-level along-shore southerly wind periods, called coastal jets (CJs). In this study, we take advantage of long-term satellite data to document the CJs characteristics over 2000–2007 and investigate its impact on upwelling. The CJ structure has a core some 100 km from the shore and a cross-shore scale of  $\sim 160$  km, and it usually lasts for several days (3–10). Its period of occurrence ranges from weekly to a few months. On the basis of covariance analyses between wind stress and sea surface temperature (SST) anomalies, it is found that CJ activity is seasonally phase locked with SST, with a peak season in August–October. The statistically dominant forcing mechanisms of the SST cooling during CJ event is a combination of seaward advection of temperature resulting from Ekman transport, air-sea heat exchange, and Ekman-driven coastal divergence. However, case studies of two events suggest a significant sensitivity of the dominant upwelling forcing mechanisms to the background conditions. For instance, the upward Ekman pumping associated with cyclonic wind stress curl is enhanced for the event with the CJ located more to the south. Although there are limitations associated with both the formulation of the heat budget and the data sets, the results illustrate the complexity of the upwelling forcing mechanisms in this region and the need for realistic high-resolution forcing fluxes. A CJ activity index is also proposed that takes into account the coastal upwelling variability, which can be used for teleconnection studies.

**Citation:** Renault, L., B. Dewitte, M. Falvey, R. Garreaud, V. Echevin, and F. Bonjean (2009), Impact of atmospheric coastal jet off central Chile on sea surface temperature from satellite observations (2000–2007), *J. Geophys. Res.*, 114, C08006, doi:10.1029/2008JC005083.

### 1. Introduction

[2] The Humboldt Current System (HCS), extending along the west coast of South America, is known as the most productive marine ecosystem in the world [e.g., *Food and Agriculture Organization*, 2004]. Off the coast of central Chile ( $36^{\circ}\text{S}$ – $26^{\circ}\text{S}$ ), the HCS is characterized by a band of cool waters that extends (on average) about 100 km from the shore. This SST pattern is mostly produced by coastal upwelling, due to offshore Ekman transport forced in turn by the very persistent low-level southerly flow along the eastern side of the South Pacific anticyclone [Shaffer *et al.*, 1999; Halpern, 2002]. Fonseca and Farias [1987] identified five principal coastal upwelling areas off the Chilean coast, one of which is near Punta Lengua de Vaca at  $30^{\circ}\text{S}$  [Montecino *et al.*, 1996; Torres *et al.*, 1999; Daneri

*et al.*, 2000; Montecino and Quiroz, 2000], where we focus the present study. In this region, upwelling exhibits seasonal variations, with a minimum during austral winter and a maximum in austral spring-summer [Strub *et al.*, 1998]. As with the currents observed off California or off Peru [Brink, 1982; Winant *et al.*, 1987; Huyer *et al.*, 1991], quasi-geostrophic variability as coastal-trapped waves can be observed at seasonal to interannual timescales in this region [Pizarro *et al.*, 2001, 2002]. Over interannual timescales, the SST off central Chile responds principally to ENSO-related changes in the wind regime of the Pacific basin [Shaffer *et al.*, 1997; Rutllant *et al.*, 2004]. At intraseasonal timescales, there has been a very few studies that documented the SST variability over central Chile although the region exhibits vigorous eddy activity [Chaigneau and Pizarro, 2005] with a clear maximum in altimetry-derived eddy kinetic energy near  $33^{\circ}\text{S}$  within 100 km from the coast [Hormazabal *et al.*, 2004]. Most studies have focused on atmospheric variability [Hormazabal *et al.*, 2004; Rutllant *et al.*, 2004; Garreaud and Muñoz, 2005] with the subsequent assumption that SST variability in this frequency band is mostly forced through Ekman pumping. As the matter of fact, the low-level winds off the coast of central Chile, which are remarkably persistent in direction (south-

<sup>1</sup>Laboratoire d'Etudes en Géophysique et Océanographie Spatiale, Toulouse, France.

<sup>2</sup>IMARPE, Callao, Peru.

<sup>3</sup>Department of Geophysics, Universidad de Chile, Santiago, Chile.

<sup>4</sup>LOCEAN, Université Pierre et Marie Curie, Paris, France.

<sup>5</sup>Earth and Space Research, Seattle, Washington, USA.

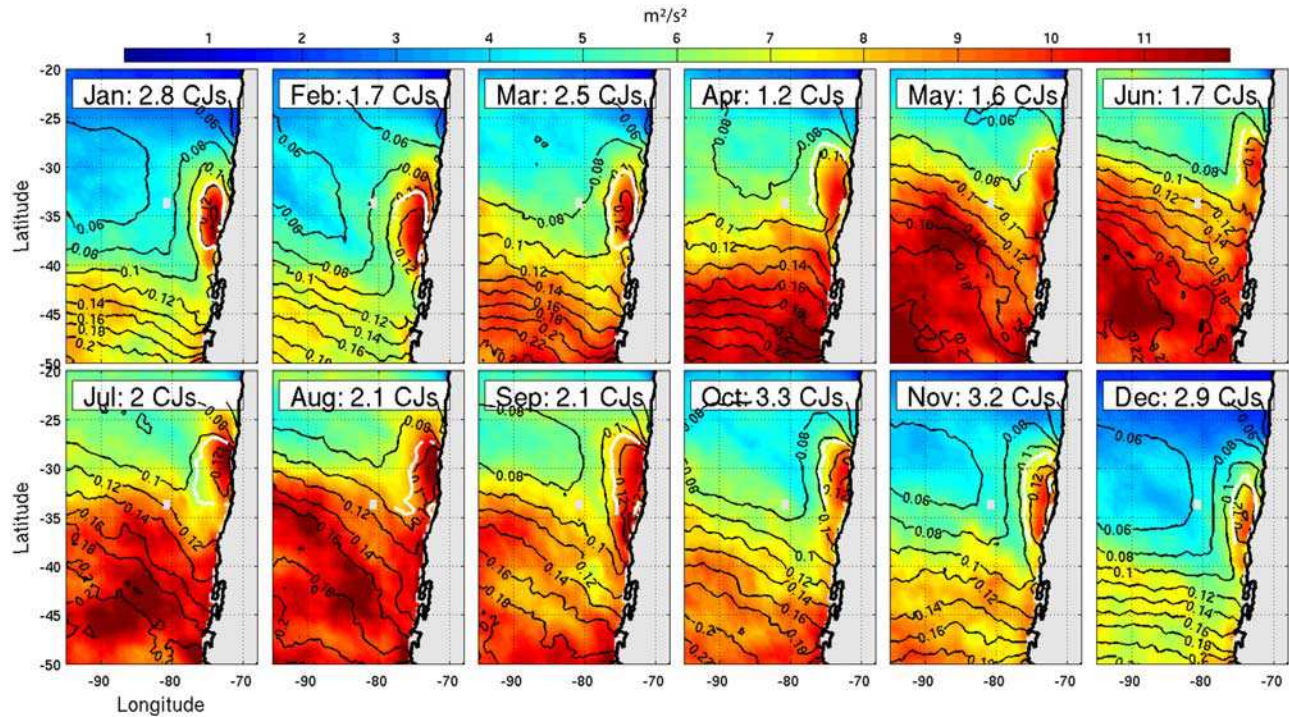


**Figure 1.** CJ activity off central Chile from QuikSCAT: climatological 15-day running variance of wind speed anomalies (colors) (unit is  $\text{m}^2 \text{s}^{-2}$ ) and climatological wind stress (contour) (in  $\text{N m}^{-2}$ ). The contour corresponding to 80% of maximum amplitude for wind stress is indicated in white. The average number of CJ for each month is indicated. For determining the average CJ number, we used a criterion of minimum wind speed of  $10 \text{ m s}^{-1}$  and a mean duration of 4.5 days.

erly) during the spring-summer months, exhibit considerable synoptic variability in their speed, principally in relation to the intermittent formation of a coastal jet (CJ) [Garreaud and Muñoz, 2005; Muñoz and Garreaud, 2005]. CJ events are forced by the passage of migratory anticyclones farther south, and may occur year round. The CJ is characterized by a meridionally elongated core of near surface southerly winds between 10 and  $15 \text{ m s}^{-1}$  (twice the climatological mean), some 300 km wide and usually centered about 100 km offshore. The coastal jet provides a particularly favorable environment for enhanced sea surface cooling but the actual forcing mechanism of the upwelling event associated to CJ remain unclear. Stronger than normal southerlies may be expected to increase offshore transport and hence coastal upwelling [Bakun and Nelson, 1991; Halpern, 2002; Rutllant et al., 2004] and the subsequent offshore advection of cool, coastal water. The CJ is also associated with stronger than normal west to east gradient in the meridional wind, conducive to offshore upwelling via Ekman pumping [Halpern, 2002]. Furthermore, the stronger winds may also enhance air-sea exchanges of sensible and latent heat and mixing within the ocean mixed layer (ML). The occurrence of CJ episodes may thus be expected to play an important role in modulating the spatial and temporal variability of the SST off central Chile over submonthly time scales.

[3] Despite ongoing efforts to develop regional observational networks, there are very few in situ oceanic observations in this region. For instance, the average frequency of

drifters near the coast of central Chile ( $90^\circ\text{W}$ – $70^\circ\text{W}$ ;  $37^\circ\text{S}$ – $28^\circ\text{S}$ ) is equivalent to about 71 drifters per year, and only 26 Argo floats entered the area over the last 6 years. Satellite observations remain the main source of information on the oceanic and atmospheric circulation in this region. However, it is not clear to what extent the available satellite data can grasp the characteristics of the intraseasonal variability at the regional scale. In this paper, we take advantage of extended satellite data sets to investigate CJ activity and its impact on sea surface temperature (SST) off central Chile. Because of inherent limitations of these data sets (resolution, blind zone, and precision), much care is required when dealing with coastal area. In the case of the CJ, the typical spatial scale of variability is of the order of  $\sim 100 \text{ km}$ , which requires the use of satellite data having a resolution of  $\sim 1/2^\circ$  at least. The Figure 1 presents the climatology of the wind stress and wind speed running variance (in contour and color, respectively) as derived from the QuikSCAT satellite data calculated over 2000–2007. A 15-day time window was used to compute the running variance. The white contour on each map highlights the CJ core zone (80% of the value of the local maximum of wind stress) and illustrates the spatial scale of variability as a function of calendar month and the seasonal change in the latitudinal location of the CJ core. Basically, two types of CJ can be identified from the QuikSCAT data: during austral summer, the CJs are centered at about  $35^\circ\text{S}$  and peak at  $0.12 \text{ N m}^{-2}$ , whereas during austral winter, the CJs are centered at about  $30^\circ\text{S}$  with weaker amplitude (maximum of  $0.10 \text{ N m}^{-2}$ ).



The cross-shore scale estimated from the best fit of a Gaussian curve on the variability maps leads to values of  $\sim 150$  km which is significantly larger than the typical Rossby radius of deformation in this region [cf. *Chelton et al.*, 1998]. All these observed features suggest that significant impact on SST through Ekman and mixed layer dynamics may be expected and that the latter may be discernable from satellite observations.

[4] The main objective of this paper is to assess if satellite observations can provide information on the underlying mechanism producing upwelling variability in this region, namely, identify the principal mechanisms that lead to the observed SST variations. This study is also viewed as a preliminary step toward implementing regional models for the coast of central Chile, which will require observational reference data for validation purposes.

[5] The paper is organized as follows: Satellite-derived data products and the few available in situ observations are described in section 2 along with the methodology used in the paper. Section 3 presents the dominant air-sea variability characteristics of CJ events based on the results of covariance analyses over 2000–2007. Section 4 focuses on two particular CJ events with different characteristics (location of the core, duration, and strength) and applies a simplified mixed layer heat budget to infer the dominant cooling process associated with them. Our results are summarized in section 5, where possibilities for future work are also discussed.

## 2. Data and Method

### 2.1. Data

#### 2.1.1. Wind Speed From QuikSCAT

[6] The near-surface atmospheric circulation over the ocean is described through daily QuikSCAT zonal and meridional wind components, obtained from CERSAT (expand CERSAT) (<http://www.ifremer.fr/cersat>) on a  $0.5^\circ \times 0.5^\circ$  latitude-longitude grid [*Centre ERS d'Archivage et de Traitement (CERSAT)*, 2002]. This product is built from both ascending and descending passes from discrete observations (available in JPL/PO.DAAC Level 2B product) over each day. Standard errors are also computed and provided as complementary gridded fields. There is no data for grid points located within 25 km of the coastline (satellite blind zone).

#### 2.1.2. TMI Sea Surface Temperature

[7] Estimates of SST were obtained from the TRMM Microwave Imager (TMI) data set produced by Remote Sensing Systems (RSS, <http://www.remss.com>). RSS provides SST twice daily on a regular  $0.25^\circ \times 0.25^\circ$  latitude-longitude grid for latitudes lower than  $38^\circ\text{S}$ . The TMI blind zone is within 50 km of the coast. The SST estimates are based mainly on emissions at 10.7 GHz, and are largely uninfluenced by cloud cover, aerosols and atmospheric water vapor [*Wentz et al.*, 2000]. However, the microwave retrievals are sensitive to (wind induced) sea surface roughness and this potential systematic error is worth bearing in mind when considering the results presented in sections 2–5. TMI comparisons with buoys give an RMS difference of about  $0.6^\circ\text{K}$  [*Wentz et al.*, 2000] due to a combination of instrumental (buoy) collocation error [*Gentemann et al.*, 2003]. Recent comparisons of the TMI SST estimates with

buoy-measured near-surface ocean temperature show that, on greater than weekly timescales, TMI SST reproduces the characteristics of the 1-m buoy-observed temperatures in the tropical Pacific [*Chelton et al.*, 2001].

#### 2.1.3. OSCAR Surface Currents

[8] Ocean surface (0–30 m) currents were obtained from the Ocean Surface Current Analysis (OSCAR) data product [*Bonjean and Lagerloef*, 2002]. OSCAR combines several satellite observations (i.e., TOPEX/POSEIDON sea surface height, QuikSCAT/SSM/I wind vectors and SST) to derive surface zonal (u) and meridional (v) currents from the sum of their Ekman (i.e., wind driven) and geostrophic components (see *Bonjean and Lagerloef* [2002] for more details). For the present study, maps of zonal and meridional currents were generated on a  $1/3^\circ \times 1/3^\circ$  (instead of the  $1^\circ \times 1^\circ$  resolution provided in the OSCAR website) with a nominal sampling interval of 5 days. The  $1/3^\circ \times 1/3^\circ$  was shown to improve the realism of the currents near the coast compared to the  $1^\circ \times 1^\circ$  resolution. Comparison with drifters data in the study zone ( $26^\circ\text{S}$ – $37^\circ\text{S}$ ;  $90^\circ\text{W}$ – $70^\circ\text{W}$ ) indicates that  $1/3^\circ \times 1/3^\circ$  resolution OSCAR data agrees relatively well with the in situ measurements from drifters. Over 1996–2006, the average correlation with the 990 available drifter measurements was 0.77 and 0.62 for the zonal and meridional components, respectively, of the current. OSCAR has a tendency of having lower variability than the in situ measurements, and the ratio  $sk = 1 - \text{RMS}(\text{drifter} - \text{OSCAR})/\text{RMS}(\text{drifter})$  is of the order of 38% and 27% for the zonal and meridional velocities, respectively). The reader is invited to refer to Appendix A for a comparison of the statistics for the drifter data and OSCAR in the studied region (see Figure A1).

#### 2.1.4. COSMOS and OCEMOS in Situ Data

[9] In situ measurements of ocean temperature were available at two permanent moorings in the study area maintained by the Programa Regional de Oceanografía Física y Climatología of the University of Concepción (<http://www.profc.udec.cl/>). One mooring (COSMOS) is located 13 km from the coast at  $71.78^\circ\text{W}$ ,  $30.3^\circ\text{S}$ , and the other (OCEMOS) is located 150 km offshore at  $73.18^\circ\text{W}$ ,  $29.99^\circ\text{S}$ . At both sites temperature is measured at 4-min intervals at several depths (COSMOS: 218, 312, 476, and 730 m; OCEMOS: 331, 542, 1398, 2509, and 3897 m). Note that all sensors are well below the climatological mixed layer depth (MLD) (see below) and the Ekman layer ( $\sim 60$  m, estimated following *Ekman* [1905]). The locations of both moorings and the surrounding bathymetry are shown in Figure 5. Opposite “Punta Lengua de Vaca,” the coastal shelf break is  $\sim 10$  km from the coast and 200 m deep. Immediately in the north, opposite Tongoy Bay, the shelf break is farther offshore ( $\sim 50$  km) with a depth between 200 and 1000 m.

#### 2.1.5. Mixed Layer Depth Climatology

[10] The MLD was estimated from the CARS climatology [*Ridgway et al.*, 2002; *Dunn and Ridgway*, 2002]. The CARS climatology provides a 3-D temperature and salinity climatology at a relatively high resolution ( $0.5^\circ \times 0.5^\circ$ ). For every mapped point, a (zonally stretched) radius was calculated that provided 400 data points at that depth. Other points were used from one standard depth above and below, if their combined XY radius, Z distance, and bathymetry-weight-distance fell within the 400-point horizontal radius.

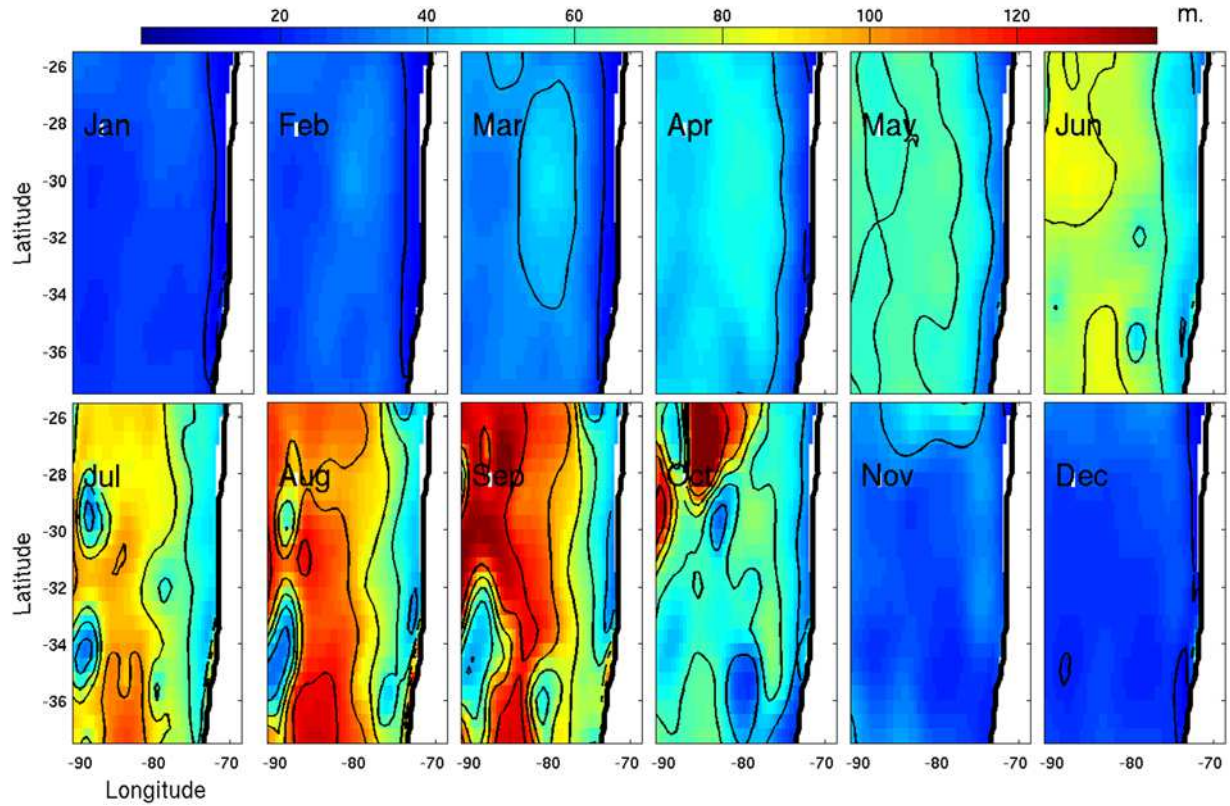


**Figure 2.** Mixing layer depth climatology from CARS along central Chile. Unit is meter. The maps were smoothed with a Whittaker's smoother using a two-grid point width boxcar average.

That is, in ocean of uniform depth, the data source region roughly forms a three-dimensional ellipse. An important characteristic of this type of mapping is that length scales are automatically adapted to data density, providing maximum resolution in areas of high sample density. A value is provided one grid point landward of the “shoreline,” allowing interpolation between grid points to locations near the shorelines.

[11] MLD was estimated from temperature using a criterion of  $0.5^{\circ}\text{C}$  which is relevant for the studied region [Takahashi, 2005]. The Figure 2 presents the estimated MLD climatology. The MLD is deeper during winter shallower during summer. It was checked that other products [de Boyer Montégut et al., 2004; Kara et al., 2003] present similar patterns in this region. The higher resolution of the CARS climatology and the specific treatment taking into account steep bathymetry led us to use the MLD derived from CARS rather than the other products.

## 2.2. Methodology

[12] Since we focus on intraseasonal variability all the fields were high-pass filtered ( $f_c = 60$  days) with a Lanczos filter. This provides what is referred as “anomalies” in the following. Other filtering methods were used that led to similar results. In particular, we tested a method which consists of removing the monthly average interpolated (using spline function) on a daily temporal grid from the total field. Such procedure was proposed for the investiga-

tion of atmospheric intraseasonal variability in the equatorial Pacific [Lin et al., 2000].

[13] Anomalies are therefore considered as deviations from a time-varying mean which corresponds to the low-frequency component of the signal. Considering a field  $X$ , we may write  $X = \bar{X} + X'$  where  $X'$  is the anomaly and  $\bar{X}$  the “mean.”

[14] A mixed layer budget is considered, whose simplicity is guided by the limitations of data sets at our disposal. As hereafter explained, only the impact of horizontal advection, heat flux (sensible and latent) and Ekman pumping is examined. Considering the above separation in mean and anomaly, the equation that governs the anomalous rate of SST changes is written as follows:

$$\frac{\partial T'}{\partial t} = - \begin{pmatrix} u' \\ v' \\ w' \end{pmatrix} \begin{pmatrix} \partial \bar{T} / \partial x \\ \partial \bar{T} / \partial y \\ \partial \bar{T} / \partial z \end{pmatrix} - \begin{pmatrix} \bar{u} \\ \bar{v} \\ \bar{w} \end{pmatrix} \begin{pmatrix} \partial T' / \partial x \\ \partial T' / \partial y \\ \partial T' / \partial z \end{pmatrix} - \text{NDH} + \frac{Q'_{\text{net}}}{\rho C_{pw} H_{\text{mix}}} + R'$$

where  $(u, v, w)$  is the 3-D velocity field,  $Q'_{\text{net}}$  the net heat flux anomalies,  $H_{\text{mix}}$  is the mixed layer depth. NDH is the nonlinear advection, also called nonlinear dynamical heating:

$$\text{NDH} = u' \frac{\partial T'}{\partial x} + v' \frac{\partial T'}{\partial y} + w' \frac{\partial T'}{\partial z}.$$

$R'$  is a residual term accounting for all the terms not taken into account in a first step.  $R'$  accounts for dissipation and mixing processes, entrainment

$$\left( \frac{\partial H_{mix}}{\partial t} \frac{[SST - T(z = H_{mix})]}{H_{mix}} \right)$$

and the low-frequency component of NDH, i.e.,

$$\overline{NDH} = u' \frac{\partial T'}{\partial x} + v' \frac{\partial T'}{\partial y} + w' \frac{\partial T'}{\partial z}.$$

It can also account to restratification process associated to mesoscale eddies [cf. *Fox-Kemper and Ferrari*, 2008]. Then  $R'$  writes as follows:

$$R' \sim \text{dissipation} + \text{mixing} - \frac{\partial H_{mix}}{\partial t} \frac{[SST - T(z = H_{mix})]}{H_{mix}} + \left[ u' \frac{\partial T'}{\partial x} + v' \frac{\partial T'}{\partial y} + w' \frac{\partial T'}{\partial z} \right] + \text{restratification}.$$

The contribution of some of the terms of  $R'$  to the rate of SST change is discussed in section 5. The variables  $\rho$  and  $C_{pw}$  are the mean density and heat capacity of the ocean water ( $\rho = 10^3 \text{ kg m}^{-3}$  and  $C_{pw} = 4.1855 \times 10^3 \text{ PSI}$ ). Note that no temperature entrainment associated with temporally varying mixed layer is considered in this budget since observed 3-D temperature is only available at seasonal timescales (CARS climatology).

[15] Because of the scarcity of data at subsurface, the vertical temperature gradient is assumed constant so that the two terms,  $w'(\partial T'/\partial z)$  and  $\bar{w}(\partial T'/\partial z)$  are not considered in the heat budget. Note that with the definition of mixed layer depth based on the temperature criteria of *Takahashi* [2005], namely,  $T(z = 0) - T(z = H_{mix}) = 0.5^\circ\text{C}$ , and the assumption of a constant mixed layer depth, the anomalous vertical gradient has to be zero. While all heat flux terms may experience some indirect relation to the changes in atmospheric and oceanic conditions associated with CJ events, the sensible and latent heat terms are expected to be especially important as their magnitude is directly related to the near surface wind velocity. Also, the net flux,  $Q'_{net}$ , are here approximated as the sum of sensible and latent heat anomalies ( $Q'_{LAT}$  and  $Q'_{SENS}$ ). Following the bulk aerodynamic formulation of *Budyko* [1963],  $Q'_{net}$  is therefore written as follows:

$$Q'_{net} = U'_{10} \rho C_E (q_{10} - q_s) + U'_{10} \rho C_H C_P (T_{10} - T_s)$$

where  $U'_{10}$ ,  $T_{10}$  and  $q_{10}$  are the wind speed anomalies, temperature and specific humidity at a nominal height of 10 m;  $q_s$  and  $T_s$  are the temperature and specific humidity at the sea surface.  $\rho$  is the air density ( $1.247 \text{ kg m}^{-3}$ ),  $\rho_w$  the water density ( $10^3 \text{ kg m}^{-3}$ ) and  $L$  is the latent heat of evaporation (2500 PSI).  $C_P$  is the air specific heat (1004.8 PSI), and  $C_E$  and  $C_H$  the turbulent exchange coefficients for sensible and latent heat  $1.5 \times 10^{-3}$  and  $1.5 \times 10^{-6}$ , respectively. Standard values for  $(q_{10} - q_s)$  and  $(T_{10} - T_s)$ ,  $1.5 \text{ g kg}^{-1}$  and  $-1^\circ\text{C}$ , respectively, were used. These values

are consistent with in situ observations over the subtropical southeast Pacific [*Garreaud et al.*, 2001].

[16] Following *Halpern* [2002], vertical velocity associated with Ekman pumping is inferred directly from wind stress:

$$w = w_E = \frac{\text{curl}(\tau)}{\rho_w f} + \frac{\beta \tau_x}{\rho_w f^2}$$

where  $\tau$  and  $\tau_x$  are the wind stress magnitude and the zonal wind stress, respectively,  $\rho_w$  is water density,  $f$  is the Coriolis parameter, and  $\beta$  is its latitudinal variation.

[17] It is possible to calculate each term of the above SST equation from the satellite data at our disposal. Considering errors associated with each data set, it is also possible to infer the error associated with each term. Details of the error calculation are given in the Appendix A.

[18] To gain insights on the physical mechanisms at work during CJ events, Singular value decomposition (SVD) analysis [*Bretherton et al.*, 1992] was used to derive the dominant statistical pattern associated to the forcing of the oceanic circulation. The SVD technique allows capturing the time/space modes that maximize the covariance between two data sets. In that sense, it is similar to an EOF (with is based on the covariance matrix of a single field), but for each modes, one obtains two time series which, if they are highly correlated, permits to regress upon the original fields to obtain the spatial patterns associated with this common temporal variability. Following *Bretherton et al.* [1992], the eigenvectors and eigenvalues of the matrix whose coefficients are the covariance between, say, wind stress and SST anomalies, are derived.

[19] Considering the fields  $S(x, y, t)$  and  $T(x, y, t)$  (for SST and wind stress), we therefore assume that  $S$  and  $T$  can be expanded in terms of a set of  $N$  vectors, called patterns [ $p_k(x, y)$ ,  $q_k(x, y)$ ], and expansion coefficients which are the associated time series of the patterns [ $a_k(t)$ ,  $b_k(t)$ ], i.e.,

$$S = \sum_{k=1}^N a_k(t) p_k(x, y) \quad \text{and} \quad T = \sum_{k=1}^N b_k(t) \cdot q_k(x, y).$$

$p_k(x, y)$  and  $q_k(x, y)$  can be written as vectors representing the patterns ( $\vec{p}_k$ ,  $\vec{q}_k$ ). The “leading” patterns  $\vec{p}_1$  and  $\vec{q}_1$  are chosen so that the projection of  $a_1(t)$  of  $S$  on  $\vec{p}_1$  has the maximum covariance with the projection  $b_1(t)$  of  $T$  on  $\vec{q}_1$ . Successive pair ( $\vec{p}_k$ ,  $\vec{q}_k$ ) are chosen in exactly the same way with the added condition that  $\vec{p}_k$  and  $\vec{q}_k$  are orthogonal to ( $\vec{p}_1, \dots, \vec{p}_{k-1}$ ) and ( $\vec{q}_1, \dots, \vec{q}_{k-1}$ ), respectively. The choice of  $\vec{p}_1$  and  $\vec{q}_1$  that will maximize this covariance is deduced from the SVD of the covariance matrix  $C = [c_{ij}]$  with  $c_{ij} = \int S(x_i, y_i, t) \cdot T(x_j, y_j, t) dt$ , where  $(x_i, y_i)$  corresponds to the points of the domain over which the SVD modes are sought. The properties of  $C$  are discussed by *Strang* [1988, pp. 443–452]. The SVD consists in the diagonalization of  $C$ . The coefficients of the diagonal matrix are the singular values, generally called squared covariance fraction, and are ranked in the usual order from largest to smallest. They represent the squared covariance accounted for by each pair of singular vectors.



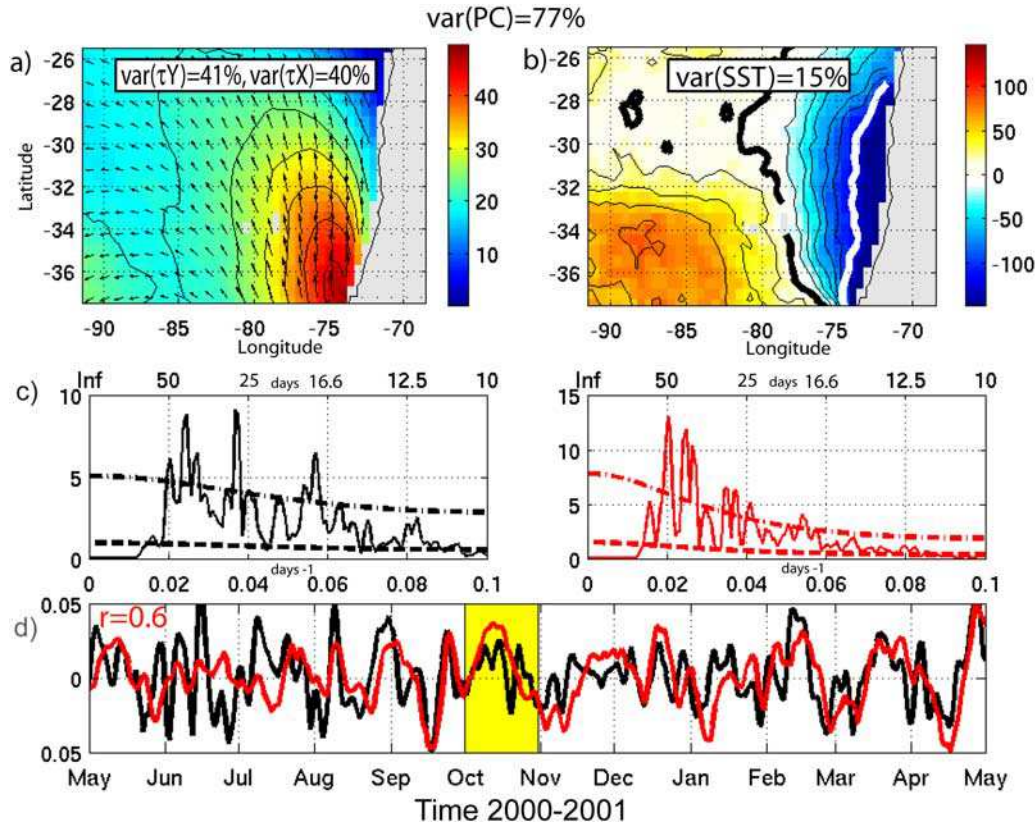


**Figure 3.** First mode of the SVD between wind stress and SST anomalies: (a) the wind speed spatial component (color) and the wind direction (arrows). (b) The SST spatial component. The black thick contour represents the zero contour, the thick white contour represents the location of the maximum SST cross-shore gradient. (c) Spectrum of the associated time series: left (right) is for the wind stress (SST). The upper (lower) scale provides the period (frequency). The dashed lines represent the 5% and 95% confidence interval estimated from a red noise (Markov). (d) The black (red) line represents the associated wind (SST) time series; only the period May 2000 to May 2001 is shown. The yellow shading highlights the October 2000 CJ.

The eigenvectors provide the mode patterns for each field that are associated to the maximum covariance. The reader is invited to refer to *Bretherton et al.* [1992] for more details on the method and to *Wallace et al.* [1992] for another application to geophysical fields.

[20] This technique is used here to derive the statistically dominant variability timescales and spatial patterns associated to the upwelling variability directly forced by the CJs (as opposed to upwelling variability originating from remote forcing in the form of coastal trapped Kelvin waves). Note that the SVD will capture a variety of variability scales within the intraseasonal frequency band which are not necessarily associated to CJ activity. In the following, for simplicity, we will refer to CJ activity all the variability scales present in the extracted dominant SVD mode considering that it explains a significant variance of wind anomalies along the coast.

### 3. CJ Air-Sea Mode

#### 3.1. SST-Related Variability

[21] As illustrated in Figure 1, CJs exhibit significant seasonal variability in both the location of its core (which

moves northward in austral winter) and its activity (more events on average in austral fall; see numbers of CJ events indicated in Figure 1). Such variability characteristics are likely to transfer to the oceanic conditions. To study the relation between coastal surface winds and SST off central Chile, the covariability of near surface wind and SST is examined. A SVD analysis on the daily SST and wind stress anomalies was performed over the domain [91°W–68°W; 38°S–26°S] for the period 2000–2007. The results for the spatial patterns and associated time series are displayed in Figure 3 and statistics are summarized in Table 1. The SVD is successful in extracting a well-defined dominant mode: The first mode accounts for 77% of the covariance and 40% and 41% of the variance in zonal and meridional wind stress, respectively. Over the entire domain, the first SST mode explains 15% of the variance, indicating a more coastally trapped spatial scale of variability than the wind stress. This value hides regional variations. In particular near the coast, the local percentage of explained by the first mode for the SST anomalies can be as high as 40% (Figure 4). The CJ as revealed by the SVD analysis has a core centered at 100 km of the coast, and presents a typical cross-shore extension of ~160 km and a meridional exten-

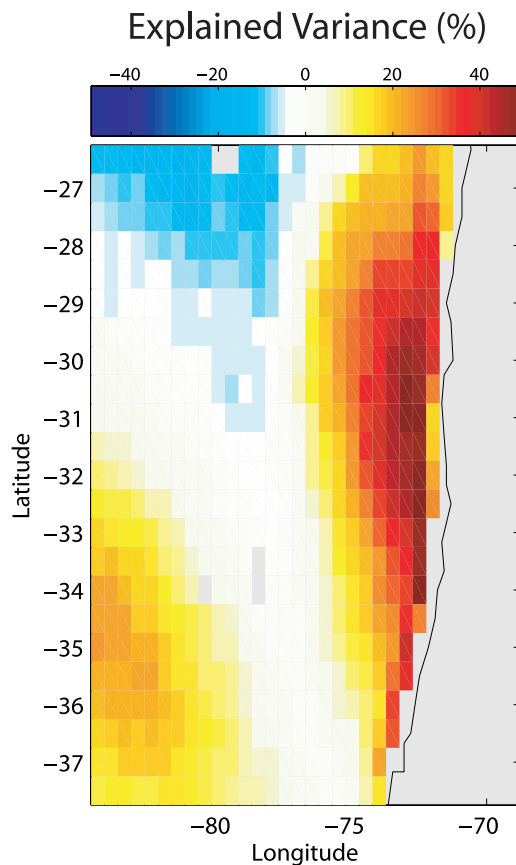


**Figure 4.** SST anomaly explained variance by the first SVD mode between wind stress and SST.

sion of 220 km (estimated by fitting a Gaussian curve on the mode patterns), consistent with the study of *Garreaud and Muñoz* [2005]. The associated SST pattern consists of a zone of maximum variability along the coast between 38°S and 26°S with cross-shore spatial scale of  $\sim 250$  km. Spectral analysis of the associated series reveals significant energy peaks at  $\sim 15$ , 18, 27, 29, and  $40 \text{ d}^{-1}$  for the wind and at  $\sim 18$ , 25, 27, 29, 40 and  $50 \text{ d}^{-1}$  for SST. The 5% and 95% interval confidence in Figure 3b was estimated by a Markov red noise [*Gilman et al.*, 1963]. The concomitant energy peaks for SST and wind stress are for frequencies centered around 15–20, 30, and  $40 \text{ d}^{-1}$ . Since CJ dynamics is linked to the large-scale synoptic variability [*Garreaud and Muñoz*, 2005], it is likely that these energy peaks correspond to peculiarities of the extratropical storm activity. In fact, there is significant variance concentrated in the 10–20 day range, which is slightly larger than the typical synoptic variability range in the midlatitudes (5–15 days). It is important to keep in mind that we are analyzing a subtropical region, so not all synoptic disturbances leads to the formation of a CJ. It is likely that one every two synoptic disturbances have the intensity and duration to force a CJ off central northern Chile. The other significant spectral peak around 40 days, which is in the limits of the range analyzed in this study, is likely to results from intra-seasonal variability rather than high-frequency, synoptically driven CJ events. It is beyond the scope of this paper to investigate such issue, but we note that such intraseasonal peak has also been detected in other studies of the SE Pacific.

For instance, *Xu et al.* [2005] found that cloud liquid water over this region exhibits a peak at 8–16 and 40–80 days. The relationship between CJ event and the large-scale low-level circulation is further discussed in section 5.

[22] The correlation between the first SVD mode time series is  $r = 0.52$  ( $\sigma = 0.95$ ) (maximum correlation is  $r = 0.60$  for a lag of 1 day, wind ahead SST) which confirms the strong relationship between CJ events and SST variability along the coast.

[23] In order to infer the seasonal dependence of covariability between wind stress and SST anomalies, the climatology of the 2-month running correlation between the time series associated with the first SVD mode is presented in Figure 5. The covariability between wind stress and SST has a marked seasonal cycle with the highest value for correlation occurring in September ( $r = 0.7$ ) when the CJs are stronger, and the lowest in June ( $r = 0.31$ ). Figure 5 clearly indicates a seasonal dependence of the upwelling-CJ relationship.

[24] The second SVD mode accounts for 15% of the covariance, and is characterized by southward winds offshore and northward winds nearshore (not shown), associated with SST heating and cooling, respectively. The correlation between PC1(SST) and PC2(SST) reaches  $-0.25$  with a lag of 4 days and most likely corresponds to a decay phase of the jet and a drop off in wind intensity.

[25] To summarize, the statistical dominant mode of covariability between wind stress and SST in the central Chile region is representative of the CJ activity. The CJ participates in SST cooling with the pattern of Figure 3 and having the largest magnitude in austral fall. The analysis also reveals a marked seasonal dependence of the upwelling-CJ relationship. The time series for wind stress as derived from the SVD will be used as an index of CJ activity in the rest of the paper.

### 3.2. Surface Current Related Variability

[26] Surface current anomalies are derived from altimetry and satellite wind stress (see section 2). It was checked that geostrophic currents contribute the most to the total current variability in this region. The percentage of explained variance of the geostrophic component of the meridional (zonal) current reached 90% (72%) on average over the studied domain. However, at the regional scale considered here, one expects that wind stress covaries more with Ekman currents than with geostrophic currents, which was checked through SVD analysis considering both components separately. The SVD between wind stress amplitude and Ekman surface currents leads to a dominant mode that

**Table 1.** Results of the Covariance Analyses for Wind Stress, SST, and Geostrophic Surface Currents

	Covariance Dominant Mode (%)	Correlation Value Between the Associated Time Series	Variance (%)
SST	77	0.52	15
$\tau_x$			40
$\tau_y$			41
$\ \vec{\tau}\ $	54	0.39	27
U			10
V			4



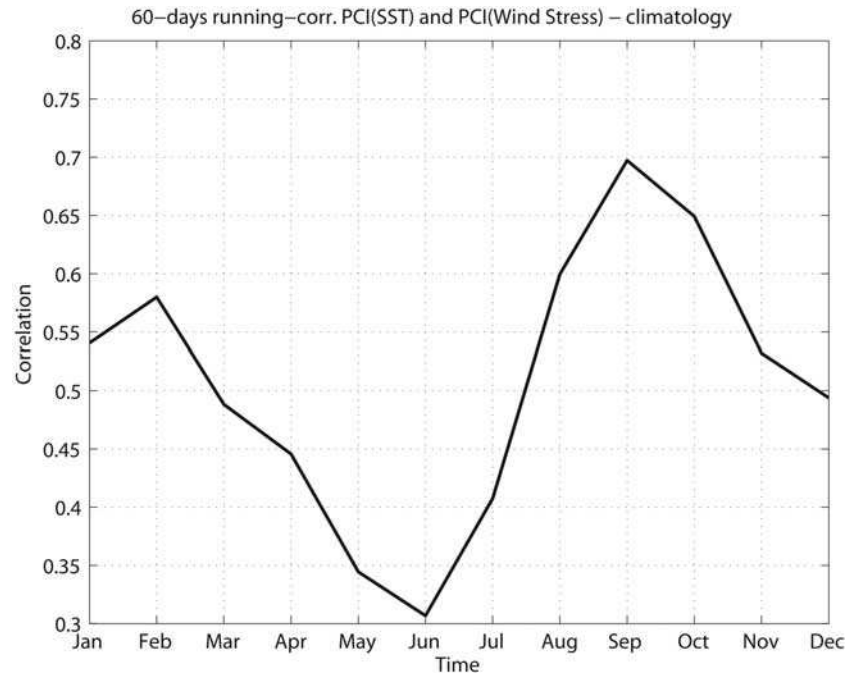


**Figure 5.** Climatology of the 60-day running correlation between the principal component for SST and wind stress. Correlation are significant at the level  $\sigma = 95\%$ .

explains 86% of the covariance (not shown). Note that this may be overestimated since OSCAR currents are derived from the QuikSCAT winds. On the other hand, the SVD between wind stress amplitude and the geostrophic component of OSCAR currents reveal interesting features. Figure 6 presents the results. The wind stress pattern of Figure 6 is similar to that of Figure 3 indicating that the covariability between wind stress and geostrophic surface currents is representative of the CJ activity. The satellite data permits the detection of a CJ-related geostrophic current that is equatorward and confined within a narrow band ( $\sim 100$  km wide) along the coast, consistent with geostrophic adjustment resulting from the shallowing of the isopycnals at the coast during upwelling, and similarly to what was observed in the upwelling off Senegal [cf. Estrade, 2006]. The CJ-related Ekman currents (contour) extend farther offshore (as far as  $\sim 500$  km, not shown). Variability timescales associated with the principal component for wind stress and surface current are similar than those in Figure 3, although with weaker values of correlation (Figure 6c). The correlation peaks in June and then decreases slightly in winter, suggesting a different response of the regional circulation to the CJ according to the season. Note that in June, CJs have less impact on SST (Figure 5).

[27] Overall, these results for surface currents indicate that satellite derived currents can grasp some aspects of the regional circulation variability relevant for the study of the impact of CJ on SST. In the following, and in the light of the above, we document the processes responsible for the SST changes during CJ event from the formerly described satellite observations.

### 3.3. Rate of SST Change: Preferential Cooling Process

[28] To understand the main cooling process during CJ events, the SVD analysis is applied to the terms of the

simplified heat budget described in section 2.2, meaning that we consider the covariability between the rate of SST changes,  $\partial T'/\partial t$ , and the different terms of the SST equation. Results are presented in Figure 7 and statistics (percentages of covariance and variance, correlation value between the principal components) are summarized in Table 2. Only the map for  $\partial T'/\partial t$  corresponding to the SVD between  $\partial T'/\partial t$  and mean horizontal advection  $[-\bar{u}(\partial T'/\partial x), -\bar{v}(\partial T'/\partial y)]$  is presented since the equivalent maps for the other SVD analyses are very similar to this one (not shown), as are their associated time series (correlation always superior to  $r = 0.9$  ( $\sigma = 0.95$ )). Interestingly the pattern for  $\partial T'/\partial t$  (Figure 7a) resembles the one for the wind stress resulting from the SVD between wind stress and SST anomalies (Figure 3a) suggesting that the SST tendency is more directly related to the thermal processes controlled by the winds, rather than those driven by the SST. The percentage of covariance of the first mode from the different SVD results, along with the correlation value between time series, is indicative of the likely contribution of each cooling process during CJ activity (see Table 2).

[29] The results indicate first that nonlinear advection (NDH, Figure 7f) is a marginal contributor to the SST changes since the SVD results give the lowest percentage of covariance and correlation between time series compared to the other tendency terms. On the other hand, cooling associated with heat loss from the ocean appears to be a significant process during CJ. However, the mode pattern associated with heat flux (Figure 7g) is centered south of the maximum of SST rate of change (Figure 7a) and has a broader spatial scale. In addition, the maximum correlation between the SVD mode time series is reached during austral summer (7–8 months ahead the peak phase of CJ activity) indicating that the seasonal change in sensible heat is associated with SST warming during summer rather than

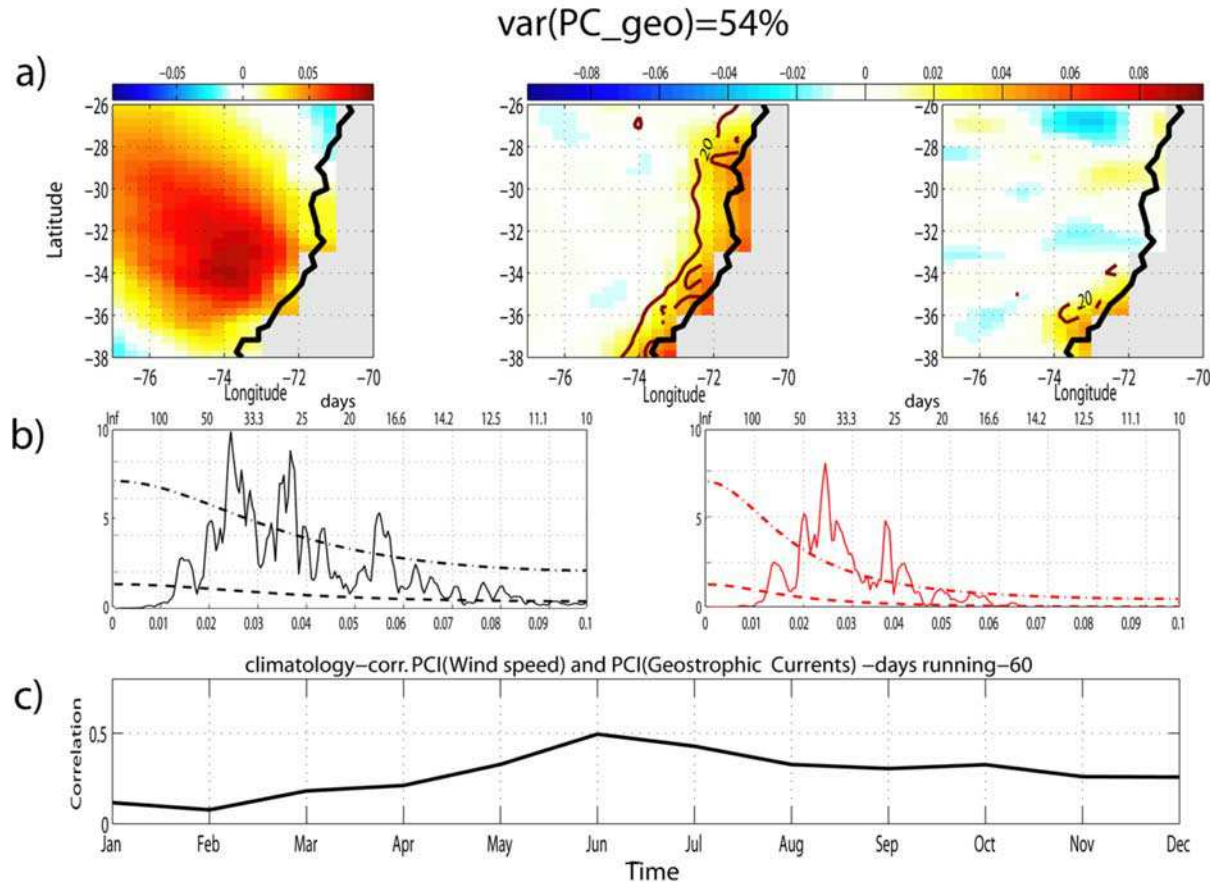


**Figure 6.** First mode of the SVD analysis between wind stress amplitude and geostrophic surface current anomalies near Coquimbo: (a) (left) spatial pattern for wind stress amplitude, (middle) meridional current anomalies, and (right) zonal current anomalies. The contours for the current patterns represent the explained variance by the SVD mode. Contour interval is every 20%. (b) Spectrum of the associated time series for wind stress (back) and total current (red). The dashed lines represent the 5% and 95% confidence interval estimated from a red noise (Markov). (c) Climatology of the 60-day running correlation between the associated PC time series. The percentage of covariance is indicated at the top. Percentages of variance of the modes for the various fields are given in Table 1.

changes in latent heat fluxes associated with wind changes. It is noteworthy that the SVD in this case is equivalent to a statistical slab-mixed layer model (i.e., a model that considers only heat flux anomalies for the SST equation), which is not likely to simulate realistic SST in a region where ocean (upwelling) dynamics is prominent. For these reasons, the results for net flux remain difficult to interpret near the coast where upwelling through Ekman pumping and transport is expected to take place. As a matter of fact, the mode patterns for horizontal advection and Ekman pumping (Figures 7b–7e and 7h) indicate a significant contribution to the cooling confined to the upwelling cell (see also percentages of covariance in Table 2). Anomalous vertical advection of mean temperature associated with Ekman pumping is confined within  $\sim 100$  km near the coast and participates in SST cooling with 11% of explained variance. Note however that the peak phase of the seasonal covariability (yellow line in Figure 7i, February) is 6 months ahead the maximum correlation for mean horizontal advection of anomalous temperature (blue line in Figure 7i), suggesting a seasonally dependant forcing mechanism through Ekman pumping associated with the CJ-SST mode.

We will investigate this possibility in the case studies in section 4. Mean meridional advection of anomalous temperature (Figure 7b) is confined within  $\sim 220$  km of the coast with minimum amplitude in the northern part of the domain whereas mean offshore advection of anomalous temperature (Figure 7c) contributes to the SST cooling in the core of the upwelling cell with a percentage of variance reaching 18%. The latitudinal variability of these contributions suggests that, near the coast, and in the core of the jet, increased Ekman pumping leads to increased upwelling that is associated through surface divergence to offshore mean advection of SST anomalies (since the SST zonal gradient near the coast is increased in absolute value). This negative SST anomaly, at first confined to the central part of the domain, may produce an anomalous meridional SST gradient that may extend the SST anomalies northward through mean meridional advection of anomalous temperature (Figure 7b). In the meantime, anomalous zonal advection of mean temperature (Figure 7e) spreads the cooling offshore as far as  $80^\circ\text{W}$ , reflecting Ekman transport. Finally, despite the existence of a geostrophic coastal jet associated with the CJ (Figure 6), anomalous meridional advection of

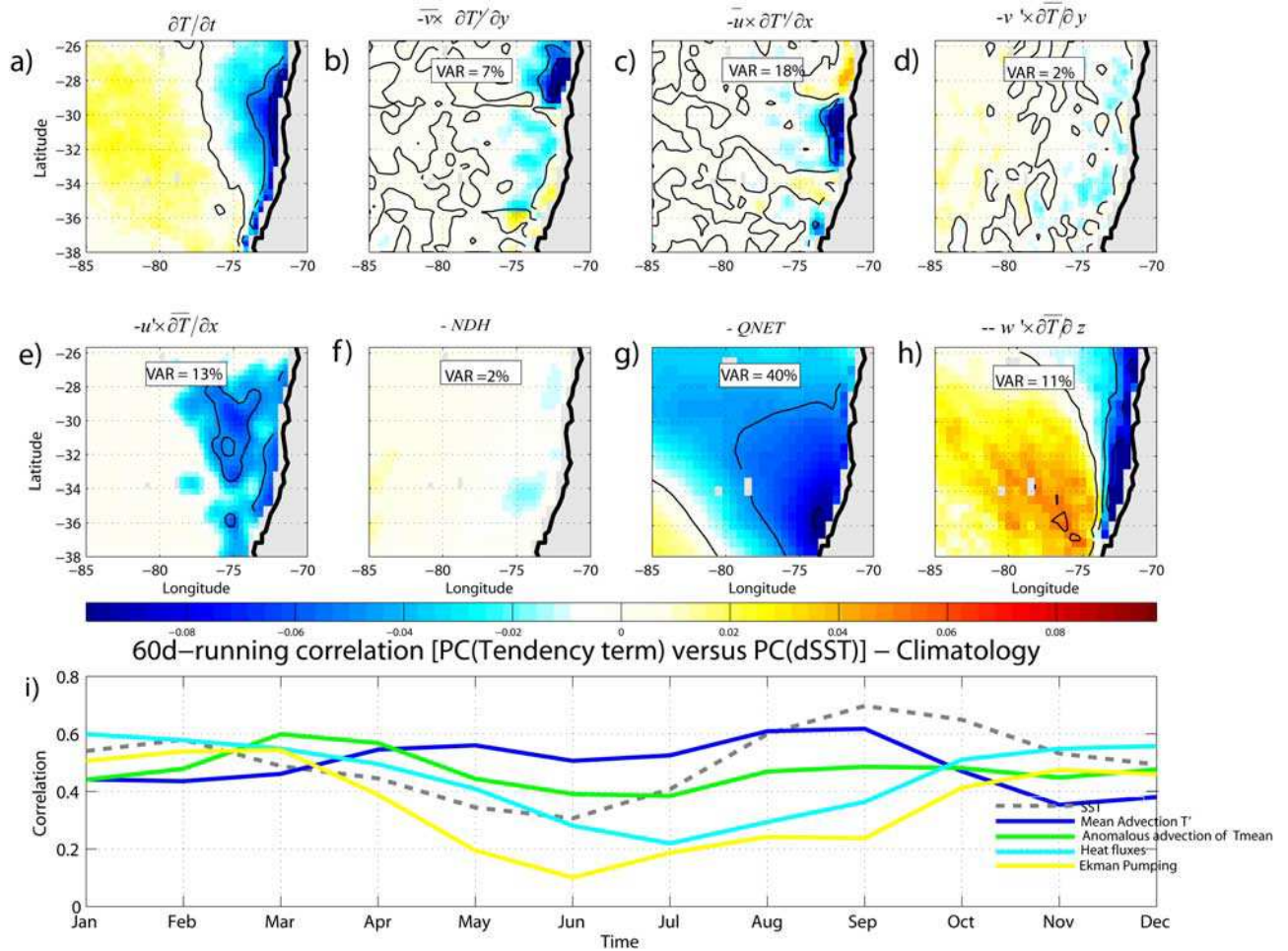


**Figure 7.** First mode of the SVD between the rate of SST change and the advection and heat flux terms (see text for details): From left to right, spatial patterns for (a)  $\partial T'/\partial t$ , (b)  $-\bar{v}(\partial T'/\partial y)$ , (c)  $-\bar{u}(\partial T'/\partial x)$ , (d)  $-\bar{v}'(\partial \bar{T}/\partial y)$ , (e)  $-\bar{u}'(\partial \bar{T}/\partial x)$ , (f)  $-NDH$ , (g)  $-Q_{NET}$ , and (h)  $-\bar{w}'(\partial \bar{T}/\partial z)$ , respectively (see text for details and notation). (i) The climatology of the 60-day running correlation between the PC time series for each SVD result (except NDH). The dashed gray line recalls the curve of Figure 5. The blue, green, cyan, and yellow lines represent the climatology for the mean horizontal advection of mean temperature, for net heat flux, and for vertical advection associated with Ekman pumping, respectively.

mean temperature has a marginal contribution to the cooling (Figure 7d). This may be due to the delayed response of the geostrophic adjustment compared to Ekman adjustment.

[30] The correlation between the SVD time series is rather high (see Table 2) for the processes of horizontal advection, which corroborates their dominant contribution to the development of the upwelling event. In order to gain insight on the timing of each process, the climatology of the running correlation between the SVD time series is estimated (Figure 7i). It indicates that the correlation for mean advection of anomalous temperature peaks at the same time than the peak phase of the coupling between SST anomalies and CJ activities (dashed gray line; from Figure 5). On the other hand the correlation for anomalous advection of mean temperature peaks in March, which suggests some seasonal dependence of the forcing mechanism of the upwelling event in relation with CJ activity.

[31] To summarize, the above statistical analysis from satellite data over 2000–2007 supports the existence of

persistent and seasonally varying CJ activity off central Chile. The imprints of the CJ in the SST data are revealed in the results of SVD analysis performed from various quantities. The SST pattern consists in a well-defined upwelling cell extending from 26°S and 33°S and from the coast as far as 250 km offshore. SST variability along the coast can be interpreted as being predominantly due to both mean horizontal advection of anomalous temperature and anomalous zonal advection of mean temperature and, to a lesser extent, to Ekman pumping whose covariability with along-shore winds peaks in austral summer, the low season for CJ activity. Farther offshore (downstream of the CJ), there is a likely larger contribution of anomalous heat fluxes. Although the SVD analysis provides a meaningful description of the air-sea interface variability associated with CJ activity, it does, by definition, hide the peculiarities of individual CJ events. In particular, as revealed by Figure 1, there is a marked seasonality in the location of the core and the amplitude of the CJ. Section 4 investigates two events with



**Table 2.** Results of the Covariance Analyses for the SST Rate of Change and Terms of the SST Equations

	Covariance Dominant Mode (%)	Correlation Value Between the Associated Time Series	Variance (%)
$\partial T/\partial t$	40	0.50	12
$-u'(\partial \bar{T}/\partial x)$			18
$-v'(\partial \bar{T}/\partial y)$			7
$\partial T/\partial t$	61	0.42	14
$-\bar{u}(\partial T'/\partial x)$			13
$-\bar{v}(\partial T'/\partial y)$			2
$\partial T/\partial t$	21	0.30	2
NDH		12	2
$\partial T/\partial t$	66	0.49	14
$Q_{NET}/\rho_o C_p H_{mix}$			40
$\partial T/\partial t$	53	0.33	12
$-w'(\partial \bar{T}/\partial z)$			11

distinct characteristics. Focusing on individual events also allows calculation of a heat budget taking into account the simultaneous contributions of all the terms of the SST equation (in contrast to the statistical approach used above).

#### 4. Case Studies: The October 2000 and January 2003 Coastal Jets

[32] Two CJ events were selected corresponding to contrasting situations in terms of intensity and extent: Figure 8 presents maps of the wind speed and SST anomalies during the periods 9–11 October 2000 and 9–12 January 2003 at the peak phase of two observed CJs. Whereas the CJ of October 2000 has a core located at 30°S, the January 2003 CJ peaks at 34°S and has a broader influence on SST, supposedly due to a larger wind stress curl forcing as evidenced by the larger zonal change in meridional stress anomalies. The following details the cooling processes associated with both events.

#### 4.1. The October 2000 CJ

##### 4.1.1. Time Evolution

[33] The October 2000 CJ is a well-defined coastal jet episode that took place from 3 to 15 October 2000 with its maxima at ~30°S. The event took place very close to mooring sites (see location of the sites on Figure 8a), and its atmospheric structure and dynamics have been described by *Muñoz and Garreaud* [2005], providing background material for the interpretation of our results.

[34] Figure 8a presents the mean surface wind speed (contour) and SST anomalies (shaded field) between 9 and 11 October which represents the CJ peak phase. As in other coastal jet events [e.g., *Garreaud and Muñoz*, 2005] there is a tongue of high southerly winds (in excess of 12 m s<sup>-1</sup>) extending from the coast toward the northwest, with the jet's core situated at 30°S and about 100 km off the coast. The pattern of Figure 8a is similar to that of the SVD mode shown in Figure 3a, although it is shifted to the north by 6°. Significant sea surface cooling is observed along the coast, mostly confined to the area of strongest wind speed (>10 m s<sup>-1</sup>). In particular, the maximum cooling (<-1.2°C) is found at 30°S within 100 km off the coast, just underneath the core of the jet.

[35] In order to follow the evolution of the CJ and its impact on the oceanic conditions, Figure 9 (top) shows the original and 4-day filtered TMI SST and daily QuikSCAT wind speed at the same offshore point (73.2°W, 30.1°S) studied by *Garreaud and Muñoz* [2005]. The wind speed increased sharply on 3 October, remained above 10 m s<sup>-1</sup> until 15 October and decreased sharply afterward. Particularly steady conditions in the intensity (~13 m s<sup>-1</sup>) and position of the jet were observed in the period 9–11 October. The meridional component (southerly winds) accounted for over 90% of the wind speed. The SST dropped by about 1.5°C from 3 October (jet onset) to 11 October and then gradually increased.

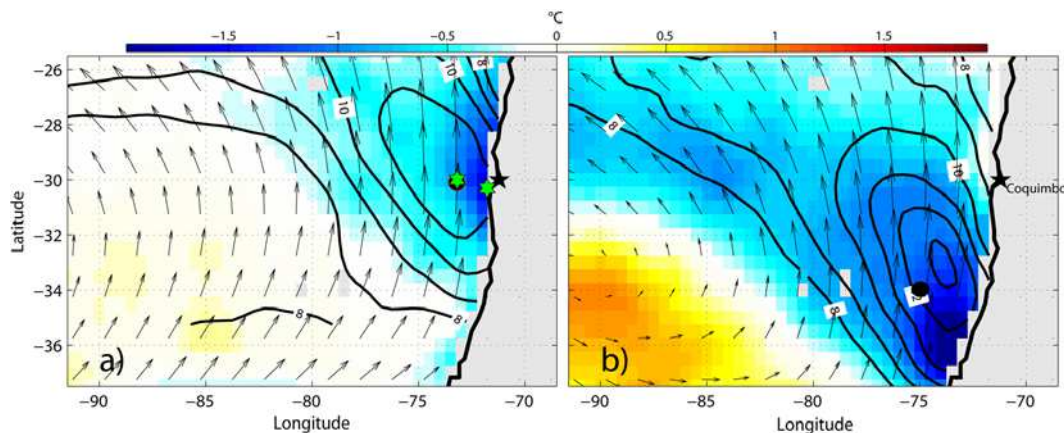


**Figure 8.** (a) Spatial structure of the SST cold anomaly related to the October 2000 CJ during the peak phase (9–11 October 2000). The shaded field indicates the mean SST anomaly during the peak phase of the CJ. The thick contours (each contour represents 1.0 m s<sup>-1</sup>) and arrows stand for the QuikSCAT surface wind speeds (m s<sup>-1</sup>) and direction, respectively. For clarity, vectors are shown every two grid points. The green stars indicate the offshore and coastal mooring sites, and the black circle indicates the location of the site studied by *Garreaud and Muñoz* [2005]. (b) Same as Figure 8a but for the January 2003 CJ during the peak phase (9–12 January 2003). The black circle indicates the location of the site where the heat budget was carried out (see Figure 11).

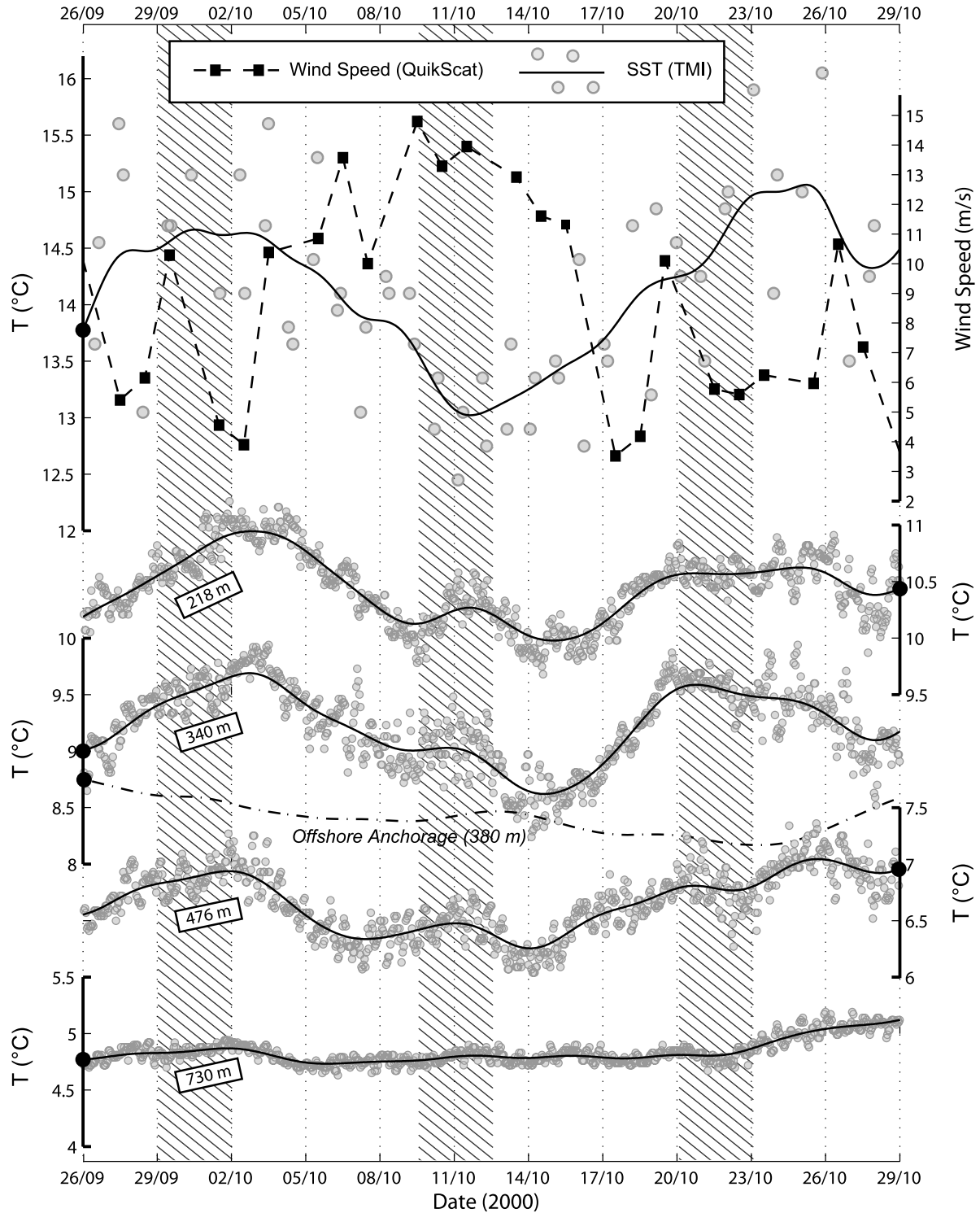


**Figure 9.** A detailed view of the temporal variation of ocean temperature and surface wind during the October 2000 coastal jet event. (top) The sea surface temperature estimated by TMI at 73.2°W, 30.1°S (gray dots). (middle) the ocean temperature measured at the nearshore mooring (gray dots) (COSMOS, see Figure 8) at depths of 218 and 340. (bottom) Same as Figure 9 (middle) at depths of 476 and 730 m. Solid lines show the temperature variation after the application of a low-pass filter ( $f_c = 3 \text{ d}^{-1}$ ). The filtered temperature variation at 380 m at the offshore mooring site (OCEMOS, dash-dotted line) is shown on the same axis as the 340 m temperature data. The daily mean QuikSCAT wind speed estimates at the same location as the TMI data are also shown (dark squares connected by dashed line).

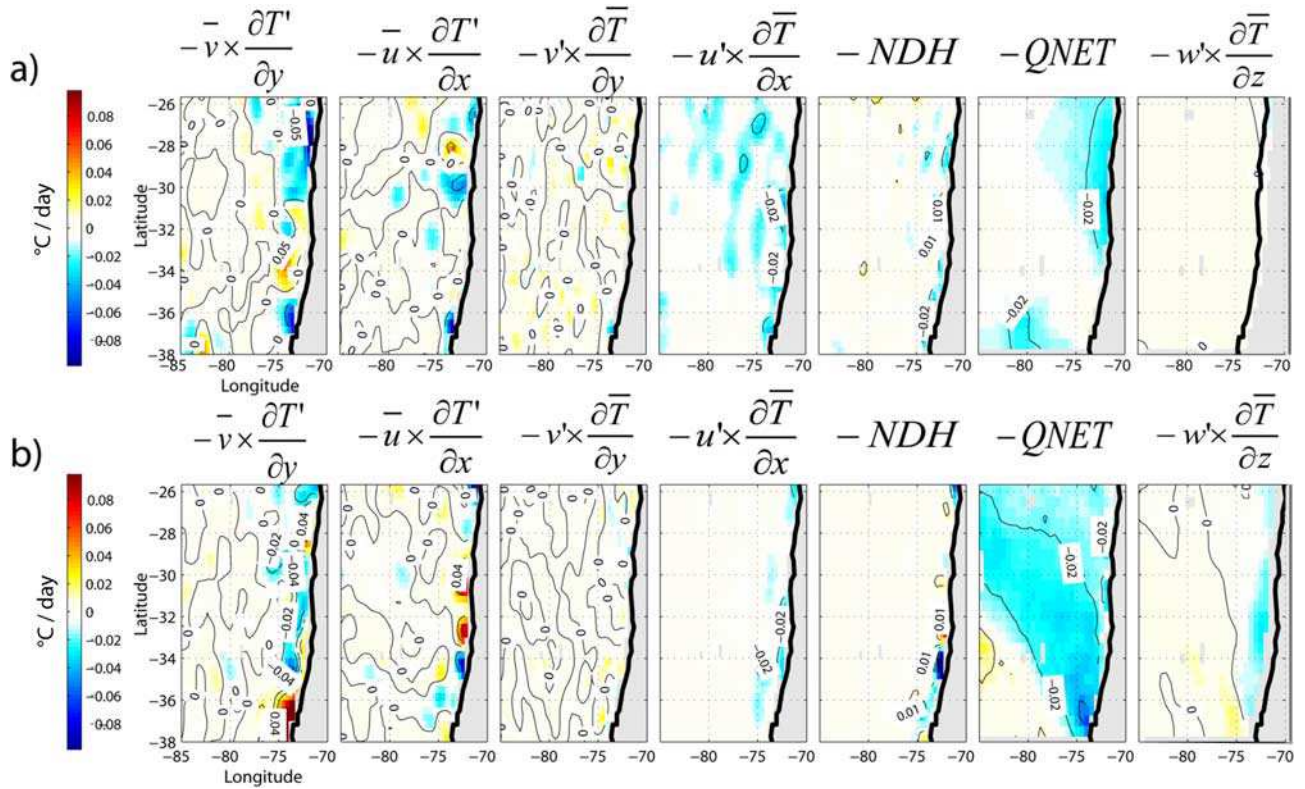


**Figure 10.** (a) Heat budget during the cooling phase of the October 2000 CJ (7–11 October 2000). Mean anomalies (colors and contours) of the advection and heat flux terms of the SST equation for (from left to right)  $-\bar{v}(\partial T'/\partial y)$ ,  $-\bar{u}(\partial T'/\partial x)$ ,  $-\bar{v}'(\partial \bar{T}/\partial y)$ ,  $-\bar{u}'(\partial \bar{T}/\partial x)$ ,  $-\text{NDH}$ ,  $-\text{Q}_{\text{NET}}$  and  $-\bar{w}'(\partial \bar{T}/\partial z)$  (see text). Units are  $^{\circ}\text{C d}^{-1}$ . (b) Same as Figure 10a but for the January 2003 CJ (the cooling phase spans the period 7–11 January 2003).

[36] The in situ data from the coastal mooring allows examination of the impact of the CJ on subsurface temperatures (Figure 9, middle and bottom). Cooling of  $1^{\circ}\text{C}$  at 218 m and 340 m, and  $0.5^{\circ}\text{C}$  at 476 m, is observed from the onset of the CJ event until its end on 15 October, followed by a more rapid warming on 16–17 October. At 730 m there is no temperature variation indicating a baroclinic response of the ocean to the CJ. Thus, while the cooling decreases with depth, we observe a correspondence between the CJ behavior and in situ temperature at the coastal site.

[37] In contrast with the observations near the coast, at the offshore mooring (OCAMOS) the ocean temperature exhibits only a weak decrease over the course of the CJ event, with no clear relation to the surface wind speed. Consistent with Figure 6a, the zonal and meridional surface current increased westward and northward, respectively, during the CJ, slightly prior to the peak phase of the event (not shown).

#### 4.1.2. Heat Budget

[38] We now investigate the mechanisms by which the CJ influences the ocean and leads to the localized SST cooling features described previously.

[39] A simplified heat flux budget similar to the one used in section 3 is considered over the period of the CJ. Figure 10a presents the maps of the different terms of the SST equations integrated over a 5-day period prior to the peak phase of the event (11 October 2000). Consistent with the results of the SVD analysis, heat fluxes, mean meridional and

zonal advection of anomalous temperature and anomalous zonal advection of mean temperature have a significant contribution to the SST cooling during this particular CJ event. Close to the coast, near  $30^{\circ}\text{S}$ , the cooling trend at the surface reaches about  $-0.04^{\circ}\text{C d}^{-1}$  ( $\pm 0.02^{\circ}\text{C d}^{-1}$ ),  $-0.05^{\circ}\text{C d}^{-1}$  ( $\pm 0.028^{\circ}\text{C d}^{-1}$ ),  $-0.02^{\circ}\text{C d}^{-1}$  ( $\pm 0.01^{\circ}\text{C d}^{-1}$ ) and  $-0.02^{\circ}\text{C d}^{-1}$  ( $\pm 0.01^{\circ}\text{C d}^{-1}$ ), respectively. NDH and vertical advection associated with Ekman pumping make only a marginal contribution to the cooling. The Figure 11a displays the time evolution of each of these terms at ( $73.2^{\circ}\text{W}$ ,  $30.1^{\circ}\text{S}$ ) along with the rate of SST change. Within the estimated range of errors (see Appendix A for the detailed calculation of the errors), the cooling at the peak phase of the October 2000 CJ can be explained to some extent ( $\sim 55\%$ ) by the summed contribution of the different processes considered here, with the meridional and zonal advection and heat fluxes making the largest contribution. The contribution of other processes, considered here in the residual of the heat budget, is discussed in section 5.

## 4.2. The January 2003 CJ

### 4.2.1. Time Evolution

[40] The January 2003 CJ is a well-defined coastal jet episode that took place from 7 to 15 January 2003 with its maxima at  $\sim 34^{\circ}\text{S}$ . The main reason for investigating the oceanic response to this event was the fact that it occurs during austral summer (favorable CJ period) and its core is



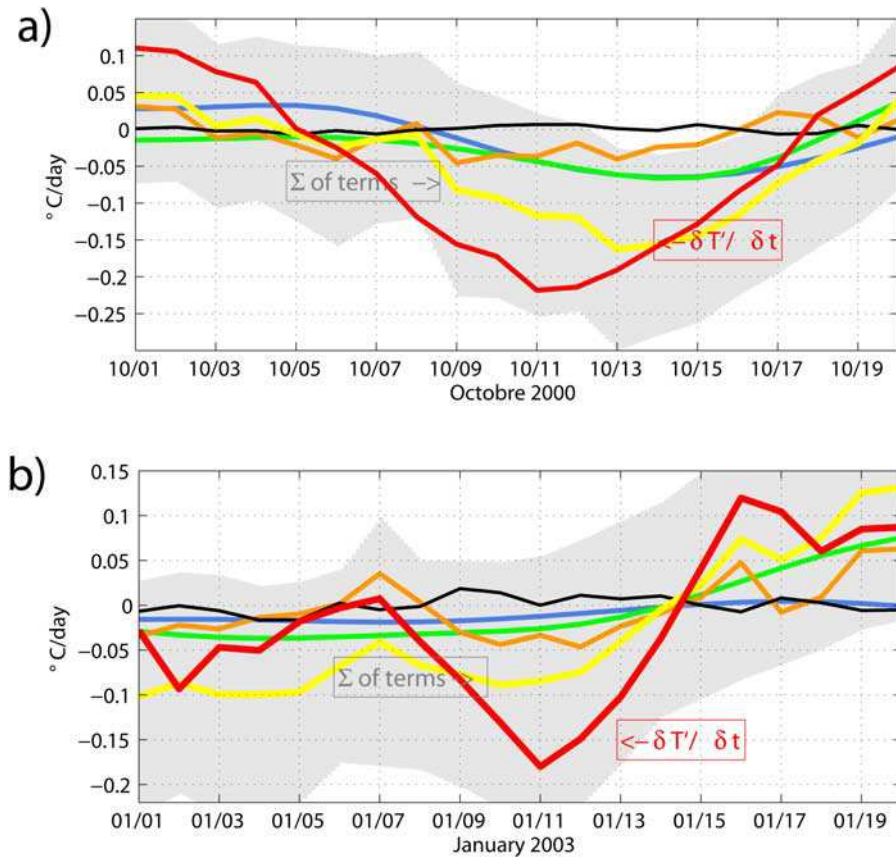


**Figure 11.** (a) Sum up of the results of the heat balance for the October 2000 CJ near ( $73.2^{\circ}\text{W}$ ,  $30.1^{\circ}\text{S}$ ). The orange, blue, green, and black lines represent the cooling rate for the heat fluxes, meridional advection, zonal advection, and vertical advection associated with the Ekman pumping, respectively. The yellow line is the summed up contribution of the advection and heat flux terms, and the gray shaded field provides the range of values allowed by the summed up contribution of the error for each term. The red line represents the SST rate of change. (b) Same as Figure 11a but for the January 2003 CJ. The location of the site is ( $75^{\circ}\text{W}$ ,  $33^{\circ}\text{S}$ ).

located near  $35^{\circ}\text{S}$  in accordance with the result of the SVD analysis (Figure 3). In that sense it is considered as a “typical” CJ.

[41] Figure 8b presents the mean surface wind speed (contour) and the SST anomalies (shaded field) averaged between 9 and 12 January (peak phase). Significant sea surface cooling is observed along the coast, mostly confined to the area of strongest wind speed ( $>10 \text{ m s}^{-1}$ ). The maximum cooling ( $<-1.5^{\circ}\text{C}$ ) is found at  $35^{\circ}\text{S}$  just underneath the core of the jet.

[42] In order to follow the evolution of the CJ and its impact on the oceanic conditions, Figure 12 shows the original and 4-day filtered TMI SST and daily QuikSCAT wind speed at the same offshore point ( $75^{\circ}\text{W}$ ,  $34^{\circ}\text{S}$ ) (see location on Figure 8b). The wind speed increased sharply on 7 January, remained above  $10 \text{ m s}^{-1}$  until 12 January and decreased sharply afterward. Particularly steady conditions in the intensity ( $\sim 12 \text{ m s}^{-1}$ ) and position of the jet were observed over the period 9–12 January. The meridional component (southerly winds) accounted for over 85% of the wind speed. The SST dropped by about  $1.1^{\circ}\text{C}$  from 7 January (jet onset) to 12 January and then gradually increased. Surface currents as seen by altimetry were also

affected (not shown). The total anomalous zonal and meridional current (dominated by the Ekman component) increased westward and northward, respectively, during the CJ.

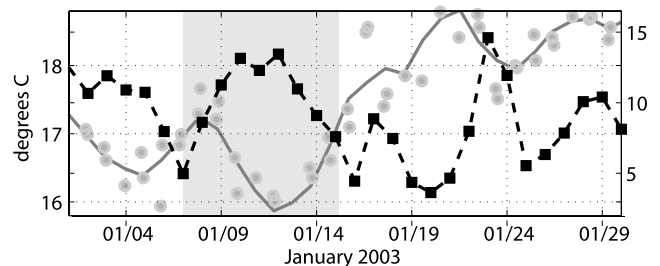


**Figure 12.** A detailed view of the temporal variation of ocean temperature and surface wind during the January 2003 CJ event. Gray dots show the sea surface temperature estimated by TMI at ( $73.2^{\circ}\text{W}$ ,  $30.1^{\circ}\text{S}$ ). Solid lines show the SST variation (a low-pass filter ( $f_c = 3 \text{ d}^{-1}$ ) was applied). The daily mean QuikSCAT wind speed estimates at the same location as the TMI data are also shown (dark squares connected by dashed line).

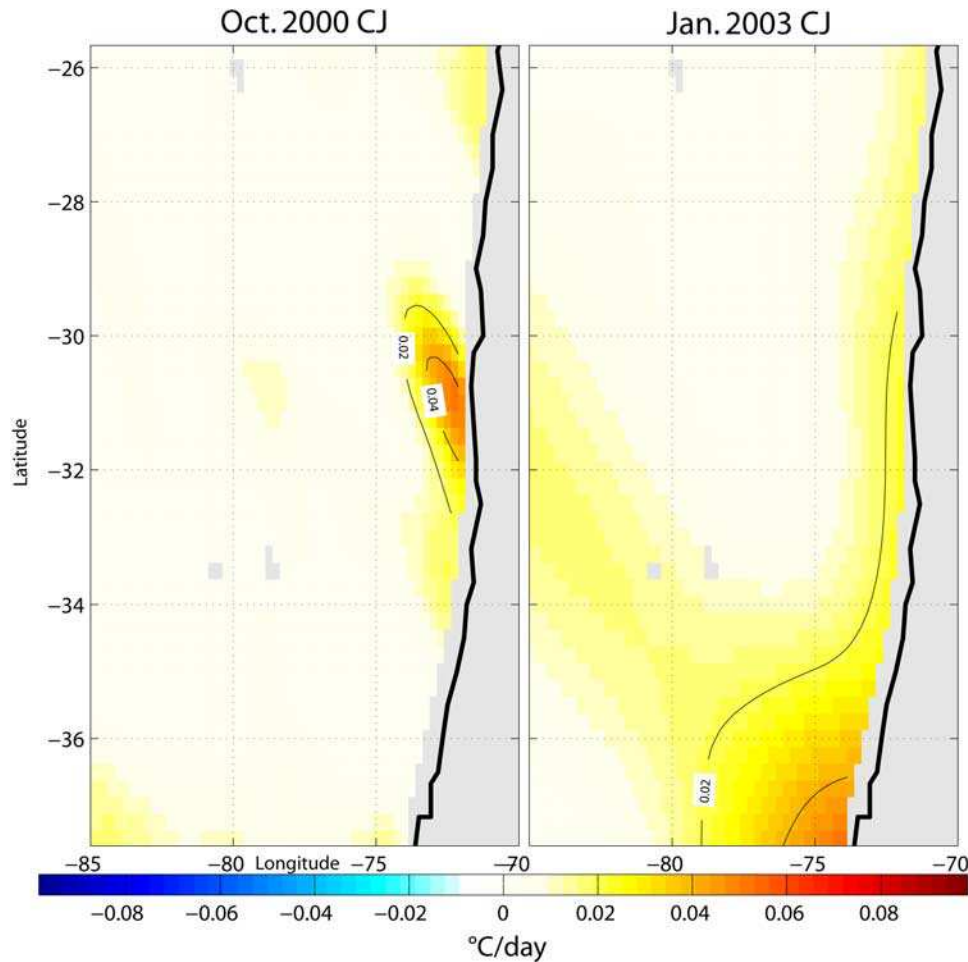


**Figure 13.** Mean tendency term associated with restratification process due to mixed layer eddies (see Appendix B) during the “warming” phase of the October 2000 and January 2003 CJ events. Units are  $^{\circ}\text{C d}^{-1}$ . Contours are every  $0.02^{\circ}\text{C d}^{-1}$ .

#### 4.2.2. Heat Budget

[43] The heat budget calculation was also applied for the January 2003 CJ. The Figure 10b presents the estimation for each term of the heat budget averaged over the 5-day period preceding the peak phase of the event (11 January 2003). Unlike the October 2000 CJ, heat flux forcing is the main contributor to the SST change, with the cooling reaching  $0.04^{\circ}\text{C d}^{-1}$ . Anomalous meridional advection of temperature and, to a lesser extent, zonal advection of anomalous temperature, also contribute to the drop in SST, although with a more localized impact. They produce a cooling trend near the coast of the order of 0.02 and  $0.015^{\circ}\text{C d}^{-1}$ , respectively.

[44] The Figure 11b displays the evolution of the SST equation terms at ( $75^{\circ}\text{W}$ ;  $34^{\circ}\text{S}$ ). Within the estimated range of errors (see Appendix A), the cooling can be explained to some extent ( $\sim 44\%$  at the peak phase) by the different processes considered here, with meridional advection and heat flux having the largest contribution.

## 5. Discussion and Conclusions

[45] On the basis of satellite data, we have documented the characteristics of coastal jet activity and its impact on

the ocean temperature off the coast of central Chile ( $35^{\circ}$ – $25^{\circ}\text{S}$ ). QuikSCAT data reveals that CJ episodes last between 3 and 10 days (average value of 4.5 days) and occur two or three times (1 or 2 times) per month during the spring-summer season (fall-winter season). Their location (maximum wind amplitude) has also a marked seasonal cycle with the winter-season (summer-season) CJ taking place at  $\sim 30^{\circ}\text{S}$  ( $35^{\circ}\text{S}$ ). During their occurrence, the surface wind speed can reach up to  $15 \text{ m s}^{-1}$  (twice the climatological mean) over a meridionally elongated region about 300 km wide and centered about 100 km from the coastline. The region between  $29$  and  $36^{\circ}\text{S}$  experiences the most frequent occurrence of CJ and encompasses two of the major upwelling areas along the Chilean coast.

[46] Covariance analyses between oceanic and wind data derived from satellite reveal that CJs off Chile have a significant impact on the regional oceanic circulation. First, CJs are associated with an upwelling cell that consists in an elongated region between  $26^{\circ}\text{S}$  and  $36^{\circ}\text{S}$  with a SST front  $\sim 220 \text{ km}$  offshore (Figure 3b). Second, and consistent with Ekman theory, CJ events are associated with offshore Ekman transport and along-shore wind-forced currents. Interestingly, the satellite data also permit the detection of the narrow along-shore equatorward oceanic jet, associated

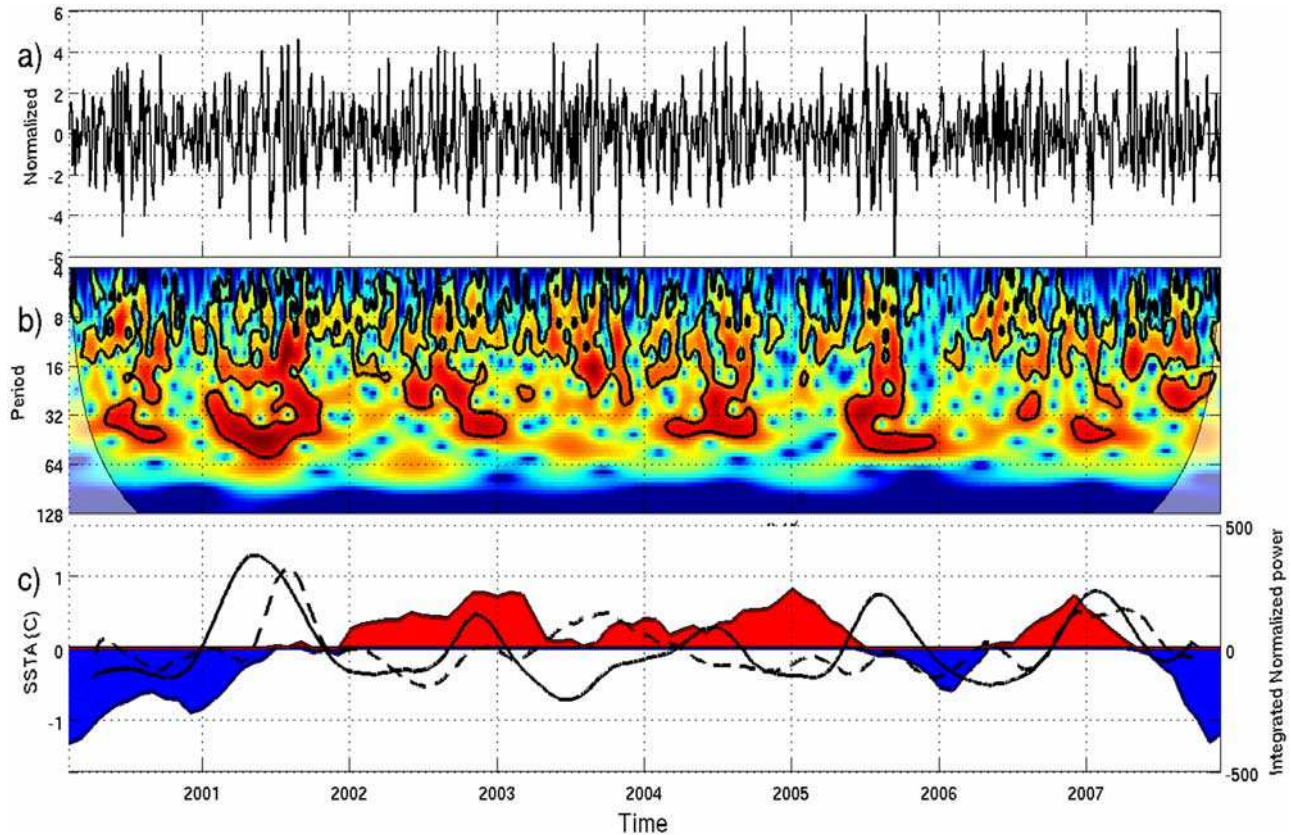


**Figure 14.** (a) Principal component for wind stress (PC1) of the results of the SVD between wind stress components and SST (Figure 3). (b) Power wavelet spectrum of PC1 using the Morlet wavelet. Contours represent values above the 95% confidence level (red noise = 0.72). (c) The scale-averaged wavelet power of PC1 over the  $[1-16] \text{ d}^{-1}$  frequency band (dashed black line) and over the  $[15-60] \text{ d}^{-1}$  frequency band (black line) and the NINO4 SST index (shaded field). The NINO4 SST index corresponds to the SST averaged in the region ( $150^{\circ}\text{E}-150^{\circ}\text{W}$ ;  $5^{\circ}\text{N}-5^{\circ}\text{S}$ ). Data are from the HadISST1 data set [Rayner *et al.*, 2003].

with the geostrophic adjustment to the cross shore density gradient induced by the shallowing of the isopycnals during upwelling event. This is consistent with numerical and observational studies of the eastern boundary systems [Hill *et al.*, 1998; Estrade, 2006]. The SVD analysis also reveals a marked seasonal cycle of the link between CJ and SST, with a peak season in austral fall (Figure 5). Within the limitations of the available satellite data sets, a simplified heat budget is proposed to document further the processes at work during the upwelling event. From a purely statistical view, it indicates that SST changes during the CJs are predominantly associated with anomalous zonal advection of mean temperature and mean zonal advection of anomalous temperature during the peak season of CJ activity (austral fall), and to heat flux forcing and Ekman-driven coastal divergence during austral summer (Figure 7).

[47] Two coastal jet events occurring in the summer and winter seasons were then investigated in detail. The October 2000 CJ was chosen because of the availability of in situ oceanic data and the existence of background material for its interpretation [Garreaud and Muñoz, 2005]. The January 2003 event was arbitrarily chosen from several well-marked summer events over 2000–2007. For the October 2000 CJ, mooring data at a site within 13 km of the Chilean coast showed a temperature variation at depth (shallower than

476 m) in phase with and of similar magnitude to the observed surface cooling. This suggests that increased offshore current transport of the upwelled waters is the primary cause of SST drop in the vicinity of the jet, which was confirmed by the northward and westward current increase observed in the OSCAR product. Moreover, heat budget calculations indicate that horizontal advection accounts for 45% ( $\pm 23.7\%$ ) of the cooling in the core of the jet during 11 October 2000. Horizontal currents transport the cold water front from the upwelling region to the open ocean. Increased latent and sensible heat flux within the CJ could contribute, to about 16% ( $\pm 10.7\%$ ) of the cooling rate in the core of the CJ for 11 October 2000. On the other hand, Ekman pumping has a negligible contribution. The January 2003 CJ has a different heat budget, with horizontal advection and anomalous heat flux having weaker contribution to the cooling (19% and 22%, respectively). The differences in the preferential cooling processes for the two events are attributed to the different mean atmospheric and oceanic conditions and to the different characteristics of the CJs (location of the core and intensity). Note that the Ekman Pumping contribution to the cooling is stronger during the January 2003 event than during the October 2000 event.

[48] We now discuss limitations of the data sets and the assumptions made for calculating the heat budget. First of



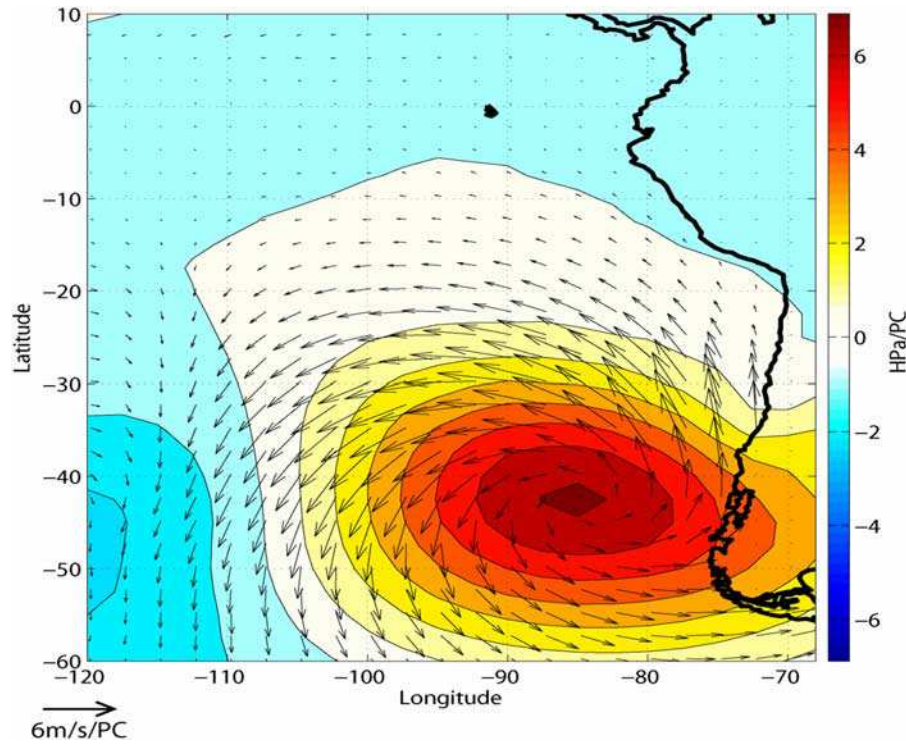


**Figure 15.** Regression map of the coastal jet index (see text for definition) onto surface pressure and the low-level circulation. Pressure is derived from the NCEP/NACR Reanalysis [Kalnay *et al.*, 1996], whereas the atmospheric circulation (velocity field) is derived from QuikSCAT. The arrows represent the regressed velocity field (scale indicated at the bottom left), and the shading is for the regressed surface pressure field.

all, the lack of subsurface data led us to consider a constant mixed layer depth although entrainment associated with a change in MLD during the CJ may take place. This is equivalent to neglecting the contribution of the term

$$\frac{\partial H_{mix}}{\partial t} \frac{[SST - T(z = H_{mix})]}{H_{mix}}$$

in the equation for the rate of SST change, which could be inappropriate. Indeed, during periods where winds are picking up and temperature drops, entrainment is likely to play a role in further reducing mixed layer temperature. The contribution of this term could be estimated by model experiment. In particular, a KPP 1-D model that has been shown to realistically reproduce mixed layer deepening through shear-driven turbulence [Large *et al.*, 1994] could be tested, which could be compared to estimates that consider the three-dimensional circulation as simulated by a high-resolution regional model. During periods where winds drop and temperature increases near-surface frontal processes lead to a restratification tendency that is thought to be significant. Such an effect can be estimated using the recent parameterization by Fox-Kemper *et al.* [2008]. The calculation of the rate of SST change induced by restratification process from SST observations and the assumptions are given in the Appendix B. The estimate of the SST changes induced by such process during the decaying phase of the CJ events is displayed in Figure 13 for the October 2000 and January 2003 CJ events. It can be

compared to Figure 10. Despite the uncertainty associated to the assumptions (see Appendix B), Figure 13 indicates that restratification associated to mixed layer eddies tends to enhance the warming trend after the peak phase of the CJ events in the region of the core of the CJs (see Figure 9), with mean tendency reaching  $\sim 0.05^\circ\text{C d}^{-1}$ . Note however, that using SST to determine horizontal density gradients tend to overestimate the fluxes because there must often be compensating salinity gradients, so that much of the small-scale SST gradient does not lead to a density gradient (B. Fox-Kemper, personal communication, 2009). In the absence of a highly sampled salinity data set, it is difficult to go further without model experiments. As regards to the horizontal diffusion of temperature,  $K_H(\partial^2 T'/\partial x^2) + K_V(\partial^2 T'/\partial y^2)$ , which is neglected in the heat budget, it has apparently a small contribution to the change in temperature within the assumptions considered here (i.e., using mean homogeneous diffusion coefficient taken from Chaigneau and Pizarro [2005]). Its contribution is less than 1% of the maximum values for the SST rate of change for the two CJs considered in the study. Again, modeling experiment could allow further refinement of the estimation of its contribution.

[49] The lack of data also leads to the assumption made for the formulation of the heat flux forcing term of the mixed layer model. Bulk formulas are used that consider changes in the wind only, although humidity and air temperature changes can have a significant impact on the heat flux variability. Moreover, the contributions of both the solar radiation and long-wave radiation to the net flux were not considered. Garreaud and Muñoz [2005] suggested that

CJ events are characterized by reduced cloudiness over the region of enhanced wind. Thus, the SST could warm due to positive solar radiation anomalies during CJ event. Note however that long-wave heat flux anomalies could compensate for this warming tendency since the contribution of the ocean to the long-wave radiation is the heat lost by blackbody radiation, and the contribution of the atmosphere is the downward infrared radiation emitted by the atmosphere (clouds in particular). Thus, clear sky coastal jets should limit the contribution of the atmosphere and cause an increase of heat lost by the ocean and as a consequence a cooling of the ocean temperature. The study of such rather subtle mechanisms will definitely require a superior observational data set or/and high-resolution regional model simulations.

[50] Finally, it is worth mentioning the limitations associated with the resolution and coverage of the data sets. The QuikSCAT satellite does not provide data in a narrow fringe along the coast, the so-called “blind zone,” so that wind stress curl for deriving Ekman pumping is not available nearshore. On the basis of a high-resolution atmospheric model, *Pickett and Paduan* [2003] have also shown that the Ekman pumping is underestimated using coarse grid products or low-resolution atmospheric models. Close to the coast, they underlined the presence of a wind drop-off zone which induces wind stress curl characteristics having the potential to drastically impact Ekman pumping. *Capet et al.* [2004] also stressed this sensitivity for the California coast from high-resolution model experiments. Modeling work needs to be undertaken to estimate the sensitivity of the upwelling response to the resolution and characteristics of the atmospheric forcing in this region. Current data also have a relatively low resolution even though they are based on the  $1/4^\circ$  resolution sea level product [*Ducet et al.*, 2000]. Recent efforts have been made to improve the mapping of these currents for regional studies since they can be valuable in regions where no in situ observing system is in place or for complementing ARGO floats or drifters data.

[51] Despite these limitations, our study illustrates the value of satellite data in documenting the atmospheric and oceanic variability at the regional scale. Along with providing insights on the mechanisms at work for producing SST changes along the coast of central Chile, satellite data can also be used for monitoring the intraseasonal variability associated with CJ events. A CJ activity index can be derived on the basis of the principal component of the result of the SVD between SST and wind anomalies derived from satellite data (Figure 3). Interestingly this index exhibits variability modulation at a wide range of time-scales, from seasonal to interannual (see Figure 14), suggesting a connection between the synoptic scale variability and the upwelling variability off central Chile. In particular, forcing of equatorial origin in the form of Kelvin waves can propagate along the coast and modify the background upwelling conditions and thereby the relative contribution of the cooling processes during CJ events discussed in this studies. Because of the rather short length of the record and the relatively weak interannual variability over 2000–2007 (see the NINO4 index on Figure 14c), it was not possible to relate the interannual equatorial Kelvin wave (as estimated from the SODA 1.4.3 Reanalysis [cf. *Dewitte et al.*, 2008]

and/or linear model simulations) with the indices of the modulation of CJ activity. Since Kelvin waves experience changes in amplitude and vertical structure during their propagation from the eastern equatorial Pacific up to central Chile, such investigation would require a proper estimation of the coastally trapped Kelvin wave characteristics at  $\sim 30^\circ\text{S}$ . This could be addressed through regional modeling. At this stage it is interesting to note that the CJ activity index is tightly linked to the large-scale synoptic variability of the midlatitudes, in particular the variability of the anticyclone of the southeastern Pacific. The Figure 15 shows the regression between the CJ activity index and the low-level circulation in the southeastern Pacific. It indicates that the CJ off central Chile and associated upwelling are driven by the passage of a migratory anticyclone over southern Chile around  $42^\circ\text{S}$ . When the center of the anticyclone is off the coast, the along-coast sea level pressure increases from north to south (opposite to the climatology, in which pressure decreases poleward). Such poleward pointing pressure gradient cannot be balanced by the Coriolis force since the presence of coastal topography (up to 1000 m above sea level (ASL)) and Andes cordillera (up to 4000 m ASL) precludes the development of zonal (cross-shore) flow in the lower troposphere. The pressure gradient then accelerates the along-shore flow (i.e., southerly winds) until turbulent mixing within the atmospheric marine boundary layer close the force balance. The inspection of the circulation at 850 hPa and pressure maps from NCEP/NCAR for the individual CJ events studied in this paper are consistent with this interpretation (not shown), confirming that upwelling intraseasonal variability along the coast of central Chile is forced by the synoptic circulation in the southeastern Pacific.

[52] Overall, our study provides background material for the understanding of the upwelling variability off central Chile that can be compared to other regions with comparable characteristics such as the central Peru coast. It can also be used for the validation and interpretation of regional high-resolution simulation. While there are ongoing efforts to develop denser regional observing systems in this region, the development of coupled oceanic-atmosphere high-resolution model is currently under consideration in order to document further the processes associated with upwelling variability in this region.

## Appendix A: Errors Estimates

[53] For the currents, following *Johnson et al.* [2007], we defined the “Oscar skill,”  $sk$ , as the ratio of the RMS difference between drifter data and OSCAR and the RMS of the drifter data ( $sk = [\text{RMS}(U_{\text{drifters}} - U_{\text{OSCAR}})/U_{\text{drifters}}]$ ). The associated error of zonal and meridional currents is then given by  $1 - sk$ . Figure A1 provides a comparison of the statistics for the drifters data and OSCAR in the studied region. OSCAR currents exhibit a good agreement with the drifter data with a skill of 0.38 (0.27) for the zonal (meridional) component. This corresponds to average errors  $\text{Err}(u) = 62\%$  and  $\text{Err}(v) = 73\%$  for the zonal and meridional currents, respectively, in the study region.

[54] Since an estimation of the horizontal SST gradient error is not available, we used instead, the standard deviation

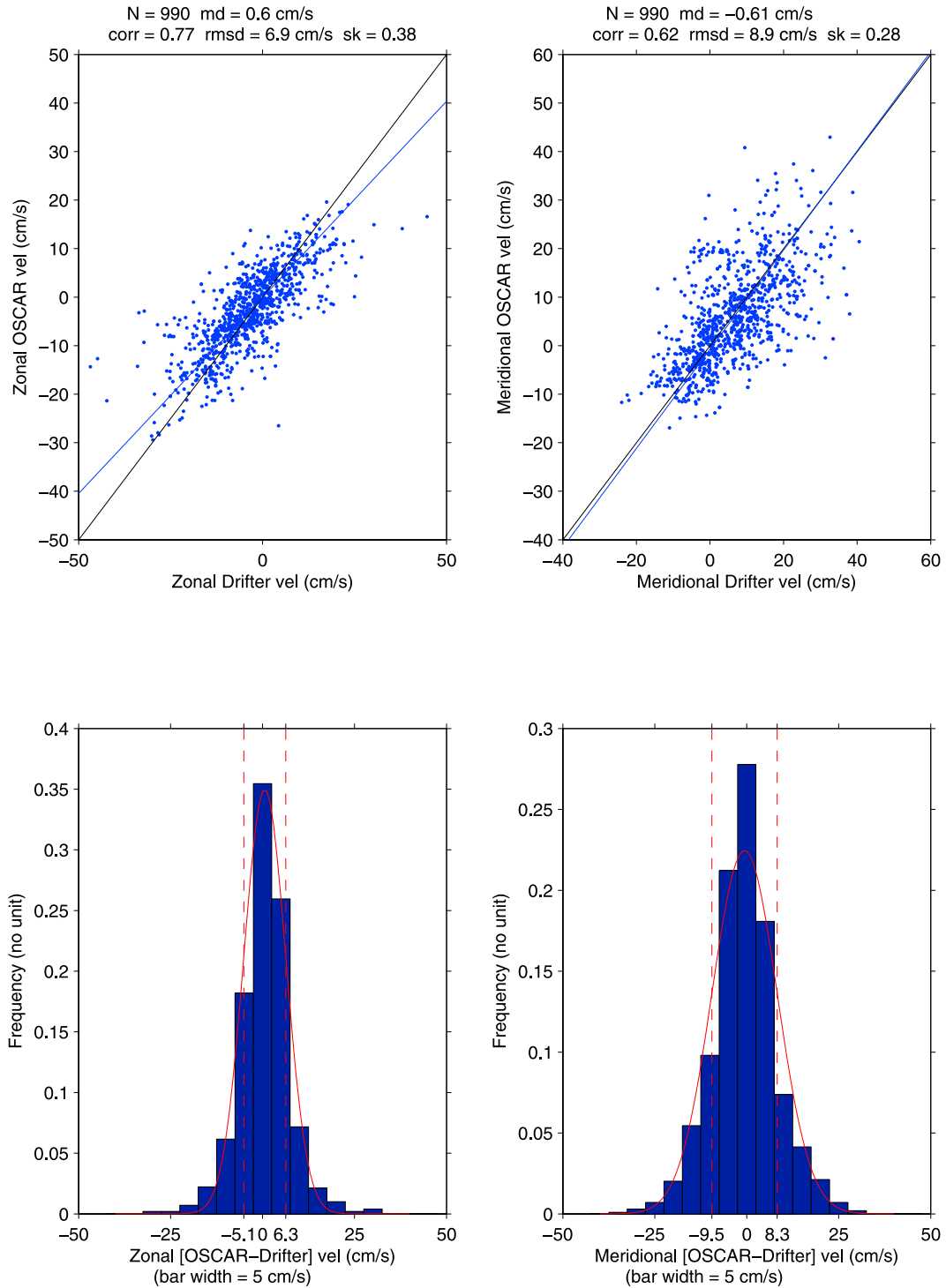


**Figure A1.** (top) Scatterplots of the drifter versus the OSCAR velocity for the region  $[80^{\circ}\text{W}-70^{\circ}\text{W}; 35^{\circ}\text{S}-25^{\circ}\text{S}]$  over the period September 1996 to November 2007. (bottom) Histograms of the difference between the OSCAR and drifter data for the same region and over the same period. The red curves are Gaussian functions plotted using the data means and standard deviations, with vertical dashed lines marking one standard deviation from the means.



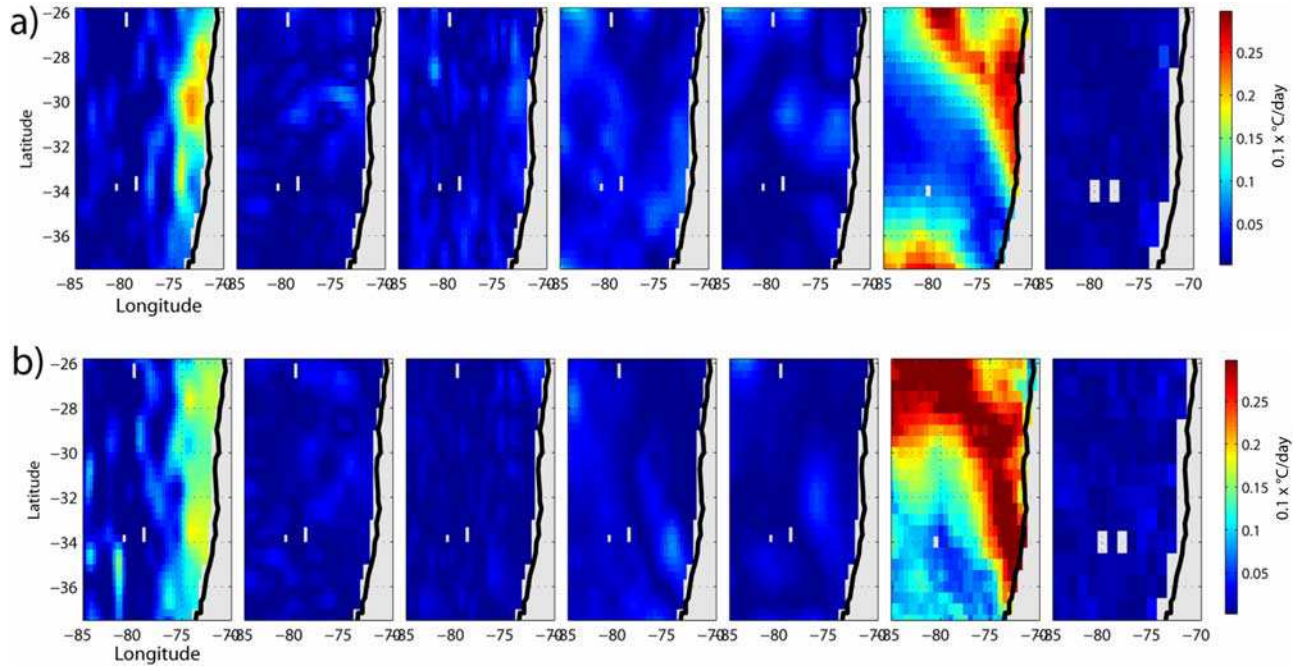


**Figure A2.** (a) Estimation of the associated error of each term of the simplified heat budget for the October 2000 CJ. Units are  $10^{-1} \text{ }^{\circ}\text{C d}^{-1}$ . The maps represent from the left to the right the spatial pattern of the error for  $\bar{v}(\partial T'/\partial y)$ ,  $\bar{u}(\partial T'/\partial x)$ ,  $v'(\partial \bar{T}/\partial y)$ ,  $u'(\partial \bar{T}/\partial x)$ , NDH,  $Q$ , and  $w'(\partial \bar{T}/\partial z)$ , respectively (see text for more details). The error corresponds to the mean error associated to the tendency term over the “cooling” phase (i.e., prior to the peak). (b) Same as Figure A2a but for the January 2003 CJ event.

tion  $\sigma$  of the high frequencies SST gradient ( $fc < 60 \text{ d}^{-1}$ ) [e.g., *Chelton et al.*, 2007]. Then, using the same notation as in section 2, the errors associated with advection are given by

[55] The results of the calculation of the errors for the two studied CJs are displayed in Figure A2, which can be compared to Figure 10.

$$\sigma \begin{pmatrix} u' \\ v' \\ w' \end{pmatrix} \begin{pmatrix} \partial \bar{T}/\partial x \\ \partial \bar{T}/\partial y \\ \partial \bar{T}/\partial z \end{pmatrix} = \text{abs} \begin{pmatrix} \text{Err}(u) \\ \text{Err}(v) \\ \sigma(w') \end{pmatrix} \begin{pmatrix} \partial \bar{T}/\partial x \\ \partial \bar{T}/\partial y \\ \partial \bar{T}/\partial z \end{pmatrix} + \text{abs} \begin{pmatrix} u' \\ v' \\ w' \end{pmatrix} \begin{pmatrix} \sigma(\partial \bar{T}/\partial x) \\ \sigma(\partial \bar{T}/\partial y) \\ \sigma(\partial \bar{T}/\partial z) \end{pmatrix}$$

$$\sigma \begin{pmatrix} \bar{u} \\ \bar{v} \\ \bar{w} \end{pmatrix} \cdot \begin{pmatrix} \partial T'/\partial x \\ \partial T'/\partial y \\ \partial T'/\partial z \end{pmatrix} = \text{abs} \begin{pmatrix} \text{Err}(u) \\ \text{Err}(v) \\ \sigma(w') \end{pmatrix} \cdot \begin{pmatrix} \partial T'/\partial x \\ \partial T'/\partial y \\ \partial T'/\partial z \end{pmatrix} + \text{abs} \begin{pmatrix} \bar{u} \\ \bar{v} \\ \bar{w} \end{pmatrix} \cdot \begin{pmatrix} \sigma(\partial T'/\partial x) \\ \sigma(\partial T'/\partial y) \\ \sigma(\partial T'/\partial z) \end{pmatrix}$$

and

$$\sigma(\text{NDH}) = \text{Err}(u) \left| \frac{\partial T'}{\partial x} \right| + \text{Err}(v) \left| \frac{\partial T'}{\partial y} \right| + \sigma(w) \left| \frac{\partial T'}{\partial z} \right| + |u'| \sigma \left( \frac{\partial T'}{\partial x} \right) + |v'| \sigma \left( \frac{\partial T'}{\partial y} \right) + |w'| \sigma \left( \frac{\partial T'}{\partial z} \right)$$

For heat flux, on the basis of the available in situ data [Garreaud *et al.*, 2001], a Monte Carlo test is carried out to derive an error associated with  $q_{10} - q_s$  and  $T_{10} - T_s$ . We find  $\text{Err}(q_{10} - q_s) = 0.3$  and  $\text{Err}(T_{10} - T_s) = 0.5$ . QuikSCAT error daily maps provided by the CERCAT are then used to derive the total error for heat flux. Those maps are also used to derive the error associated with Ekman pumping.

## Appendix B: Estimation of Restratification From SST

[56] The vertical flux associated to restratification was estimated from observations using the parameterization proposed by *Fox-Kemper et al.* [2008]. We use a similar methodology as did *Fox-Kemper and Ferrari* [2008, section 3] that estimates the vertical heat flux due to MLE restratification from observations, except that they use altimetry for deriving the horizontal buoyancy gradient instead of SST.

[57] We wish to estimate the contribution of restratification to the rate of SST change, namely,

$$\frac{\partial T'_{restrat}}{\partial t} = -\frac{\overline{\partial w' T'}}{\partial z} \approx -\frac{1}{g\alpha_T} \frac{\overline{\partial w' b'}}{\partial z}$$

with  $b' = g\alpha_T T'$  ( $\alpha_T$  was computed following McDougall [1987] for values for temperature corresponding to the mean climatological temperature in the region of the core of the CJ, i.e.,  $\sim 15.5^\circ\text{C}$ ), where the maximum value of  $w' T'$  occurs at the middepth of the mixed layer. The term  $w' \cdot b'$  is the vertical heat flux due to mixed layer eddy (MLE) restratification [see Fox-Kemper and Ferrari, 2008]. Following the notation of Fox-Kemper and Ferrari [2008], the double overline indicates horizontal averaging onto the grid of the coarse model, and primes denote submesoscale perturbations. In our case, a resolution of  $0.25^\circ$  is used so that a grid cell is a  $0.25^\circ \times 0.25^\circ$  square.

[58] Following the parameterization of Fox-Kemper, this leads to

$$\frac{\partial T'_{restrat}}{\partial t} = -\frac{\overline{\partial w' b'}}{g\alpha_T \partial z} = -\frac{C_e H^2 |\nabla \overline{b^{xy}}|^2}{g\alpha_T |f|} \frac{\partial [\mu(z)]}{\partial z},$$

where  $\mu(z)$  is the vertical structure function of the overturning stream function associated to the MLE restratification. It is provided by Fox-Kemper et al. [2008] [see also Fox-Kemper and Ferrari, 2008, equation (4)].

[59] Considering again that temperature is uncompensated by salinity:

$$\nabla \overline{b^{xy}} \approx g\alpha_T \nabla T'$$

(Note that since the coastal jet impact on SST has a rather uniform meridional extension (see Figure 3b), it is expected that buoyancy horizontal gradients are dominated by the zonal component, so that  $\nabla \overline{b^{xy}} \approx (\partial \overline{b^{xy}} / \partial x) \approx -g\alpha_T (\partial T' / \partial x)$ ).

[60] Therefore,

$$\frac{\partial T'_{restrat}}{\partial t} = -\frac{g\alpha_T C_e H^2}{|f|} \left[ \frac{\partial T'}{\partial x} + \frac{\partial T'}{\partial y} \right]^2 \frac{\partial \mu}{\partial z}$$

We use  $C_e = 0.06$  [cf. Fox-Kemper and Ferrari, 2008],  $f = 1.45 \times 10^{-4} \text{ s}^{-1} \sin(\text{latitude})$  and  $g = 9.81 \text{ m s}^{-2}$ ;  $\partial T' / \partial x + \partial T' / \partial y$  is derived from TMI;  $\partial \mu / \partial z$  is taken for  $z = 0$  (at the surface). From equation (9) of Fox-Kemper and Ferrari [2008], one derives

$$\frac{\partial \mu}{\partial z}(z=0) = -\frac{104}{21H}$$

$H$  is the mixed layer depth at the peak phase of the event. In this absence of ML data during the periods of the CJ events, the climatological values are used.

[61] **Acknowledgments.** TMI data are produced by Remote Sensing Systems and sponsored by the NASA Earth Science REASON DISCOVER Project. The QuikSCAT were obtained from CERSAT, at Ifremer, Plouzané (France). We thank the OSCAR Project Office for the OSCAR product and

Kathleen Dohan from Earth and Space Research, who helped produce the  $1/3$  degree resolution OSCAR data set. The in situ data moorings were obtained from the Programa de Oceanografía Física y Clima (PROFC) de la Universidad de Concepción. Boris Dewitte is grateful for financial support received from the French-Chilean project ECOS-Sud CO3UO5. Lionel Renault benefited from an ATUPS grant provided by the University Paul Sabatier (Toulouse, France), and from a Ph.D. scholarship received from the Centre National d'Etude Spatiale (CNES) and the Institut Français de Recherche pour l'Exploitation de la Mer (Ifremer). He is grateful to Boris Dewitte for his support during the course of his Ph.D. and for his help writing this paper. We would like to thank Yves duPenhoat (Director of LEGOS, Toulouse), who was instrumental in initiating this study, and Baylor Fox-Kemper for his help estimating change in SST associated to restratification induced by mixed layer eddies. Discussions with Xavier Capet and Ken Takashi are acknowledged. We are also grateful to Alexis Chaigneau for constructive comments on an earlier version of the manuscript. The two anonymous reviewers are thanked for their constructive comments.

## References

- Bakun, A., and C. S. Nelson (1991), The seasonal cycle of wind stress curl in sub-tropical eastern boundary current regions, *J. Phys. Oceanogr.*, **21**, 1815–1834, doi:10.1175/1520-0485(1991)021<1815:TSCOWS>2.0.CO;2.
- Bonjean, F., and G. S. E. Lagerloef (2002), Diagnostic model and analysis of the surface currents in the tropical Pacific ocean, *J. Phys. Oceanogr.*, **32**, 2938–2954, doi:10.1175/1520-0485(2002)032<2938:DMAAOT>2.0.CO;2.
- Bretherton, C. S., C. Smith, and J. M. Wallace (1992), An intercomparison of methods for finding coupled patterns in climate data, *J. Clim.*, **5**, 541–560, doi:10.1175/1520-0442(1992)005<0541:AIOMFF>2.0.CO;2.
- Brink, K. H. (1982), A comparison of long coastal trapped wave theory with observations off Peru, *J. Phys. Oceanogr.*, **12**, 897–913, doi:10.1175/1520-0485(1982)012<0897:ACOLCT>2.0.CO;2.
- Budyko, M. I. (1963), *Atlas of the Heat Balance of the Earth*, 69 pp., Academic, San Diego, Calif.
- Capet, X. J., P. Marchesiello, and J. C. McWilliams (2004), Upwelling response to coastal wind profiles, *Geophys. Res. Lett.*, **31**, L13311, doi:10.1029/2004GL020123.
- Centre ERS d'Archivage et de Traitement (CERSAT) (2002), Mean wind fields (MWF product) user manual, 1, QuikSCAT, Rep. C2-MUT-W-04-IF, Ifremer, Plouzané, France.
- Chaigneau, A., and O. Pizarro (2005), Eddy characteristics in the eastern South Pacific, *J. Geophys. Res.*, **110**, C06005, doi:10.1029/2004JC002815.
- Chelton, D. B., R. A. de Szoeke, M. G. Schlax, K. El Naggar, and N. Siwertz (1998), Geographical variability of the first baroclinic Rossby radius of deformation, *J. Phys. Oceanogr.*, **28**, 433–460, doi:10.1175/1520-0485(1998)028<0433:GVOTFB>2.0.CO;2.
- Chelton, D. B., S. K. Esbensen, M. G. Schlax, N. Thum, M. H. Freilich, F. J. Wentz, C. L. Gentemann, M. J. McPhaden, and P. S. Schopf (2001), Observations of coupling between surface wind stress and sea surface temperature in the eastern tropical Pacific, *J. Clim.*, **14**, 1479–1498, doi:10.1175/1520-0442(2001)014<1479:OOCBSW>2.0.CO;2.
- Chelton, D. B., M. G. Schlax, and R. M. Samelson (2007), Summertime coupling between sea surface temperature and wind stress in the California Current System, *J. Phys. Oceanogr.*, **37**, 495–517, doi:10.1175/JPO3025.1.
- Daneri, G., F. Dellarosa, R. A. Qiones, B. Jacob, P. Montero, and O. Ulloa (2000), Primary production and community respiration in the Humboldt Current System off Chile and associated oceanic areas, *Mar. Ecol. Prog. Ser.*, **197**, 41–49, doi:10.3354/meps197041.
- de Boyer Montégut, C., G. Madec, A. S. Fischer, A. Lazar, and D. Iudicone (2004), Mixed layer depth over the global ocean: An examination of profile data and a profile-based climatology, *J. Geophys. Res.*, **109**, C12003, doi:10.1029/2004JC002378.
- Dewitte, B., S. Purca, S. Illig, L. Renault, and B. Giese (2008), Low frequency modulation of the intraseasonal equatorial Kelvin wave activity in the Pacific Ocean from SODA: 1958–2001, *J. Clim.*, **21**, 6060–6069, doi:10.1175/2008JCLI2277.1.
- Ducet, N., P. Y. Le Traon, and G. Reverdin (2000), Global high-resolution mapping of ocean circulation from the combination of T/P and ERS-1/2, *J. Geophys. Res.*, **105**, 19,477–19,498, doi:10.1029/2000JC900063.
- Dunn, J. R., and K. R. Ridgway (2002), Mapping ocean properties in regions of complex topography, *Deep Sea Res., Part I*, **49**(3), 591–604.
- Ekman, V. W. (1905), On the influence of the Earth's rotation on ocean currents, *Arch. Math. Astron. Phys.*, **2**, 1–52.
- Estrade, P. (2006), Mécanisme de décollement de l'upwelling sur les plateaux continentaux larges et peu profond d'Afrique du Nord-Ouest, thèse de doctorat, 135 pp., Univ. de Bretagne Occidentale, Brest, France.

- Fonseca, T., and M. Farias (1987), Estudio del proceso de surgencia en la costa chilena utilizando percepción remota, *Invest. Pesq.*, **34**, 3346–3351.
- Food and Agriculture Organization (2004), Situation mondiale des pêches et de l'aquaculture 2004, *Rep.* 92-5-205177-5, Rome.
- Fox-Kemper, B., and R. Ferrari (2008), Parameterization of mixed layer eddies. II: Prognosis and impact, *J. Phys. Oceanogr.*, **38**, 1166–1179, doi:10.1175/2007JPO3788.1.
- Fox-Kemper, B., R. Ferrari, and R. W. Hallberg (2008), Parameterization of mixed layer eddies. I: Theory and diagnosis, *J. Phys. Oceanogr.*, **38**, 1145–1165, doi:10.1175/2007JPO3792.1.
- Garreaud, R., and R. Muñoz (2005), The low-level jet off the subtropical west coast of South America: Structure and variability, *Mon. Weather Rev.*, **133**, 2246–2261, doi:10.1175/MWR2972.1.
- Garreaud, R., J. Rutllant, J. Quintana, J. Carrasco, and P. Minnis (2001), CIMAR-5: A snapshot of the lower troposphere over the southeast subtropical Pacific, *Bull. Am. Meteorol. Soc.*, **82**, 2193–2207, doi:10.1175/1520-0477(2001)082<2193:CASOTL>2.3.CO;2.
- Gentemann, C. L., C. J. Donlon, A. Stuart-Menteth, and F. J. Wentz (2003), Diurnal signals in satellite sea surface temperature measurements, *Geophys. Res. Lett.*, **30**(3), 1140, doi:10.1029/2002GL016291.
- Gilman, D. L., F. J. Fuglister, and J. M. Mitchell Jr. (1963), On the power spectrum of 'red noise', *J. Atmos. Sci.*, **20**, 182–184, doi:10.1175/1520-0469(1963)020<0182:OTPSON>2.0.CO;2.
- Halpern, D. (2002), Offshore Ekman transport and Ekman pumping off Peru during the 1997–1998 El Niño, *Geophys. Res. Lett.*, **29**(5), 1075, doi:10.1029/2001GL014097.
- Hill, A. E., B. M. Hickey, F. A. Shillington, P. T. Strub, K. H. Brink, E. D. Barton, and A. C. Thomas (1998), Eastern ocean boundaries coastal segment (e), in *The Sea*, vol. 11, *The Global Coastal Ocean: Regional Studies and Syntheses*, edited by A. R. Robinson and K. H. Brink, pp. 29–67, John Wiley, New York.
- Hormazabal, S., G. Shaffer, and O. Leth (2004), Coastal transition zone off Chile, *J. Geophys. Res.*, **109**, C01021, doi:10.1029/2003JC001956.
- Huyer, A., M. Knoll, T. Paluszkiwicz, and R. L. Smith (1991), The Peru Undercurrent: A study in variability, *Deep Sea Res.*, **38**, Suppl. 1, 247–279.
- Johnson, E. S., F. Bonjean, G. S. E. Lagerloef, J. T. Gunn, and G. T. Mitchum (2007), Validation and error analysis of OSCAR sea-surface currents, *J. Atmos. Oceanic Technol.*, **24**(4), 688–701, doi:10.1175/JTECH1971.1.
- Kalnay, E., et al. (1996), The NCEP/NCAR 40-Year Reanalysis Project, *Bull. Am. Meteorol. Soc.*, **77**(3), 437–472, doi:10.1175/1520-0477(1996)077<0437:TNYRP>2.0.CO;2.
- Kara, A. B., P. A. Rochford, and H. E. Hurlburt (2003), Mixed layer depth variability over the global ocean, *J. Geophys. Res.*, **108**(C3), 3079, doi:10.1029/2000JC000736.
- Large, W., J. McWilliams, and S. Doney (1994), Oceanic vertical mixing: A review and a model with a nonlocal boundary layer parameterization, *Rev. Geophys.*, **32**, 363–403, doi:10.1029/94RG01872.
- Lin, J. W.-B., J. Neelin, and D. Zeng (2000), Maintenance of tropical variability: Impact of evaporation-wind feedback and midlatitude storms, *J. Atmos. Sci.*, **57**, 2793–2823, doi:10.1175/1520-0469(2000)057<2793:MOTIVI>2.0.CO;2.
- McDougall, T. J. (1987), Neutral surfaces, *J. Phys. Oceanogr.*, **17**, 1950–1964, doi:10.1175/1520-0485(1987)017<1950:NS>2.0.CO;2.
- Montecino, V., and D. Quiroz (2000), Specific primary production and phytoplankton size structure in an upwelling area off the coast of Chile (30°S), *Aquat. Sci.*, **62**, 364–380, doi:10.1007/PL00001341.
- Montecino, V., G. Pizarro, and D. Quirz (1996), Dinámica fitoplanctónica en el sistema de surgencia frente a Coquimbo (30°S) a través de la relación funcional entre fotosíntesis e irradianza ( $P - I$ ), *Gayana Oceanol.*, **4**, 139–151.
- Muñoz, R., and R. Garreaud (2005), Dynamics of the low-level jet off the subtropical west coast of South America, *Mon. Weather Rev.*, **133**, 3661–3677, doi:10.1175/MWR3074.1.
- Pickett, M. H., and J. D. Paduan (2003), Ekman transport and pumping in the California Current based on the U.S. Navy's high-resolution atmospheric model (COAMPS), *J. Geophys. Res.*, **108**(C10), 3327, doi:10.1029/2003JC001902.
- Pizarro, O., A. J. Clarke, and S. Van Gorder (2001), El Niño sea level and currents along the South American coast: Comparison of observations with theory, *J. Phys. Oceanogr.*, **31**, 1891–1903, doi:10.1175/1520-0485(2001)031<1891:ENOSLA>2.0.CO;2.
- Pizarro, O., G. Shaffer, B. Dewitte, and M. Ramos (2002), Dynamics of seasonal and interannual variability of the Peru-Chile Undercurrent, *Geophys. Res. Lett.*, **29**(12), 1581, doi:10.1029/2002GL014790.
- Rayner, N. A., D. E. Parker, E. B. Horton, C. K. Folland, L. V. Alexander, D. P. Rowell, E. C. Kent, and A. Kaplan (2003), Global analyses of sea surface temperature, sea ice, and night marine air temperature since the late nineteenth century, *J. Geophys. Res.*, **108**(D14), 4407, doi:10.1029/2002JD002670.
- Ridgway, K. R., J. R. Dunn, and J. L. Wilkin (2002), Ocean interpolation by four-dimensional least squares—Application to the waters around Australia, *J. Atmos. Oceanic Technol.*, **19**(9), 1357–1375, doi:10.1175/1520-0426(2002)019<1357:OIBFDW>2.0.CO;2.
- Rutllant, J., I. Masotti, J. Calderon, and S. Vega (2004), A comparison of spring coastal upwelling off central Chile at the extremes of the 1996–1997 ENSO cycle, *Cont. Shelf Res.*, **24**, 773–787, doi:10.1016/j.csr.2004.02.005.
- Shaffer, G., O. Pizarro, L. Djurfeldt, S. Salinas, and J. Rutllant (1997), Circulation and low-frequency variability near the Chile coast: Remotely forced fluctuations during the 1991–1992 El Niño, *J. Phys. Oceanogr.*, **27**, 217–235, doi:10.1175/1520-0485(1997)027<0217:CALFVN>2.0.CO;2.
- Shaffer, G., S. Hormazabal, O. Pizarro, L. Djurfeldt, and S. Salinas (1999), Seasonal and interannual variability of currents and temperature over the slope off central Chile, *J. Geophys. Res.*, **104**, 29,951–29,961, doi:10.1029/1999JC900253.
- Strang, G. (1988), *Linear Algebra and Its Applications*, 505 pp., Harcourt, Brace and Jonanovitch, San Diego, Calif.
- Strub, P. T., V. Montecino, J. Rutllant, and S. Salinas (1998), Coastal ocean circulation off western south America, in *The Sea*, vol. 11, *The Global Coastal Ocean: Regional Studies and Syntheses*, edited by A. R. Robinson and K. H. Brink, pp. 273–314, John Wiley, New York.
- Takahashi, K. (2005), The annual cycle of heat content in the Peru Current region, *J. Clim.*, **18**, 4937, doi:10.1175/JCLI3572.1.
- Torres, R., D. R. Turner, N. Silva, and J. Rutllant (1999), High short-term variability of CO<sub>2</sub> fluxes during an upwelling event off the Chilean coast at 30°S, *Deep Sea Res., Part I*, **46**, 1161–1179, doi:10.1016/S0967-0637(99)00003-5.
- Wallace, J. M., C. Smith, and C. S. Bretherton (1992), Singular value decomposition of wintertime sea surface temperature and 500-mb height anomalies, *J. Clim.*, **5**, 561–576, doi:10.1175/1520-0442(1992)005<0561:SVDOWS>2.0.CO;2.
- Wentz, F. J., C. Gentemann, D. Smith, and D. Chelton (2000), Satellite measurements of sea surface temperature through clouds, *Science*, **288**, 847–850, doi:10.1126/science.288.5467.847.
- Winant, C. D., R. C. Beardsley, and R. E. Davis (1987), Moored wind, temperature and current observations made during Coastal Ocean Dynamics Experiments 1 and 2 over the northern California shelf and upper slope, *J. Geophys. Res.*, **92**, 1569–1604, doi:10.1029/JC092iC02p01569.
- Xu, H., S.-P. Xie, and Y. Wang (2005), Subseasonal variability of the southeast Pacific stratus cloud deck, *J. Clim.*, **18**, 131–142, doi:10.1175/JCLI3250.1.

F. Bonjean, Earth and Space Research, 2101 Fourth Avenue, Suite 1310, Seattle, WA 98121, USA.

B. Dewitte and L. Renault, Laboratoire d'Etudes en Géophysique et Océanographie Spatiale, 18, Avenue Edouard Belin, F-31401 Toulouse CEDEX 9, France. (bxd@legos.obs-mip.fr)

V. Echevin, LOCEAN, Université Pierre et Marie Curie, B 101-T. 45, Etages 3-4-5, 4, place Jussieu, F-75252 Paris CEDEX 05, France.

M. Falvey and R. Garreaud, Department of Geophysics, Universidad de Chile, Blanco Encalada 2002, Santiago, Chile.